Published March 30, 2015

This article has original data in the JCB Data Viewer
http://jcb-dataviewer.rupress.org/jcb/browse/9706

A formin-nucleated actin aster concentrates cell wall hydrolases for cell fusion in fission yeast

Omaya Dudin,[1] Felipe O. Bendezú,[1] Raphael Groux,[1] Thierry Laroche,[2] Arne Seitz,[2] and Sophie G. Martin[1]

[1]Department of Fundamental Microbiology, Faculty of Biology and Medicine, University of Lausanne, 1015 Lausanne, Switzerland
[2]Bioimaging and Optics Core Facility, Ecole Polytechnique Fédérale de Lausanne (EPFL), 1015 Lausanne, Switzerland

Cell–cell fusion is essential for fertilization. For fusion of walled cells, the cell wall must be degraded at a precise location but maintained in surrounding regions to protect against lysis. In fission yeast cells, the formin Fus1, which nucleates linear actin filaments, is essential for this process. In this paper, we show that this formin organizes a specific actin structure—the actin fusion focus. Structured illumination microscopy and live-cell imaging of Fus1, actin, and type V myosins revealed an aster of actin filaments whose barbed ends are focalized near the plasma membrane. Focalization requires Fus1 and type V myosins and happens asynchronously always in the M cell first. Type V myosins are essential for fusion and concentrate cell wall hydrolases, but not cell wall synthases, at the fusion focus. Thus, the fusion focus focalizes cell wall dissolution within a broader cell wall synthesis zone to shift from cell growth to cell fusion.

Introduction

Cell–cell fusion is a fundamental process that occurs in many cell types during development and underlies sexual reproduction. Two fundamental principles may be generally valid (Shilagardi et al., 2013): First, fusogenic machineries are required to drive cell fusion upon plasma membrane contact, though their molecular nature has been identified in only few instances (Aguilar et al., 2013). Second, the actin cytoskeleton is essential for cell fusion in many cell types, such as osteoclasts, myoblasts, or yeast cells (Abmayr and Pavlath, 2012). The actin cytoskeleton may promote the juxtaposition of the two plasma membranes through precise cell polarization. This has been best described during myoblast fusion, where Arp2/3 complex–assembled actin structures in the two fusing cells drive cell–cell fusion (Kim et al., 2007; Massarwa et al., 2007; Richardson et al., 2007; Sens et al., 2010). In one of the fusing cells, this structure may generate force for membrane protrusion into the partner cell to permit fusogen engagement (Shilagardi et al., 2013).

A function for the actin cytoskeleton in fusion has also been revealed in the fission yeast *Schizosaccharomyces pombe*, in which a dedicated formin protein, Fus1, is essential for cell fusion. Cell fusion of haploid yeast cells of opposite mating types occurs after pheromone-mediated sexual differentiation to form a diploid zygote (Merlini et al., 2013). Fus1 is induced upon pheromone signaling, localizes to the fusion site, and is essential for cell fusion: indeed, *fus1* mutant cells fail to degrade the cell wall at the site of contact and instead keep elongating. Thus, fusion fails completely when both partners lack *fus1* and is inefficient in crosses with wild-type partners (Petersen et al., 1995, 1998b). Like other formins, Fus1 nucleates linear actin filaments and efficiently uses profilin-bound actin (Scott et al., 2011). Accordingly, Cdc3 profilin localizes to the fusion site and is required for fusion (Petersen et al., 1998a). In addition, Cdc8 tropomyosin, which decorates and stabilizes formin-assembled actin structures in mitotic cells (Skoumpla et al., 2007), also localizes to the fusion site and is required for fusion (Kurahashi et al., 2002). Finally, the type V myosin motors Myo51 and Myo52 are involved in cell fusion. Type V myosins transport cargoes toward the barbed end of linear actin filaments: in mitotic cells, Myo52 carries vesicular cargoes along actin cables toward cell poles, whereas Myo51 decorates these same cables as well as the cytokinetic ring (Lo Presti and Martin, 2011; Lo Presti et al., 2012; Wang et al., 2014). During sexual reproduction, both motors localize to the fusion site, and overexpression of the Myo51 cargo-binding domain leads to cell fusion defects (Doyle et al., 2009). In combination, these data suggest the existence, during cell fusion, of a Fus1-nucleated actin structure

Correspondence to Sophie G. Martin: sophie.martin@unil.ch

Abbreviations used in this paper: CHD, calponin homology domain; LatA, Latrunculin A; MSL, minimal sporulation liquid; sfGFP, superfolder GFP; SIM, structured illumination microscopy.

© 2015 Dudin et al. This article is distributed under the terms of an Attribution–Noncommercial–Share Alike–No Mirror Sites license for the first six months after the publication date (see http://www.rupress.org/terms). After six months it is available under a Creative Commons License (Attribution–Noncommercial–Share Alike 3.0 Unported license, as described at http://creativecommons.org/licenses/by-nc-sa/3.0/).

Supplemental Material can be found at:
http://jcb.rupress.org/content/suppl/2015/03/25/jcb.201411124.DC1.html
Original image data can be found at:
http://jcb-dataviewer.rupress.org/jcb/browse/9706

The Rockefeller University Press $30.00
J. Cell Biol. Vol. 208 No. 7 897–911
www.jcb.org/cgi/doi/10.1083/jcb.201411124

THE JOURNAL OF CELL BIOLOGY

Downloaded from jcb.rupress.org on March 31, 2015

Published March 30, 2015

composed of linear actin filaments. However, investigation of F-actin organization on fixed cells has so far only revealed accumulation at the fusion site of actin patches, which are Arp2/3-nucleated structures at sites of endocytosis (Petersen et al., 1998a; Kurahashi et al., 2002; Kovar et al., 2011).

Precise remodeling of the cell wall is required to allow plasma membrane contact and cell fusion between walled cells, such as yeasts. Indeed, these cells are under strong positive turgor pressure relative to their environment and are protected from lysis by their cell wall. Thus, the local dissolution of the cell wall required for cell–cell fusion must be critically controlled to bring plasma membranes into contact at a precise location, while maintaining cell wall integrity in surrounding regions. Major components of the yeast cell wall are glucan polymers, which are synthetized by transmembrane glucan synthases and hydrolyzed by secreted glucanases (Pérez and Ribas, 2004). In *Saccharomyces cerevisiae*, deletion of two glucanases was shown to compromise fusion efficiency (Cappellaro et al., 1998). How cell wall dissolution for fusion may be focalized to a specific site is unknown.

Two major ideas have been proposed from work in the budding yeast. A recent study suggested that concentration of glucanases for cell wall dissolution is achieved through restricted diffusion in the cell wall at the site of mating partner contact, rather than by a specialized fusion machinery (Huberman and Murray, 2014). In contrast, earlier work has shown that vesicles are highly aligned and clustered in a small region at the site of fusion, suggesting localized release of fusion components (Gammie et al., 1998). For this, both a fusion-specific transmembrane protein Fus1 (unrelated to its fission yeast formin Fus1 namesake) as well as Spa2, a formin-binding factor, are required (Gammie et al., 1998). Further, the Cdc42-interacting protein Fus2, also necessary for cell wall digestion, displays a focused localization at the fusion site, which relies on both Fus1- and actin-based transport (Paterson et al., 2008; Sheltzer and Rose, 2009; Ydenberg et al., 2012). The precise role of the actin cytoskeleton has not been defined, though the formin Bni1, tropomyosin Tpm1, and type V myosin Myo2 are all required for cell fusion (Liu and Bretscher, 1992; Dorer et al., 1997; Sheltzer and Rose, 2009). The tight localization of fusion factors and vesicles suggests the existence of a specific mechanism to focalize cell wall digestion for fusion.

Here, we show that the formin Fus1 nucleates a novel actin structure in fission yeast, which we named the actin fusion focus. The fusion focus consists of an aster of actin filaments whose barbed ends are focalized at a membrane-proximal site. Fusion focus focalization relies on both the formin Fus1 and type V myosins and occurs asynchronously in the two partner cells. We further show that type V myosins are essential for cell fusion and serve to concentrate in the fusion focus cell wall glucanases within a broader region of cell wall synthases to drive local cell wall dissolution for cell fusion.

Results

The fusion focus: A specific Fus1-dependent actin structure

To examine the role of the actin cytoskeleton during cell–cell fusion, we localized F-actin in live cells, using a GFP–calponin homology domain (CHD) reporter construct (Karagiannis et al., 2005; Martin and Chang, 2006). GFP-CHD has been used to study actin structures during mitotic growth, labeling the three actin structures present in these cells: the cytokinetic actin contractile ring nucleated by the formin Cdc12, actin cables assembled by the formin For3, and actin patches, which require Arp2/3 activity (Kovar et al., 2011). Strikingly, during sexual differentiation, we observed an intense accumulation of F-actin at the site of fusion (Fig. 1 A), which appeared distinct from these known actin structures. This structure dynamically formed before cell fusion, which we define as the time of entry in the h^- cell of tdTomato driven by an h^+ cell-specific promoter (p^{map3}*:tdTomato*), and decreased after fusion (Fig. 1, A and D; and Video 1). F-actin accumulation was also observed using Life-Act-GFP in live cells and phalloidin staining on fixed samples (Fig. S1). Disruption of F-actin by treatment with Latrunculin A (LatA), added 4 h after initiation of sexual differentiation upon nitrogen starvation, reduced fusion efficiency in a dose-dependent manner (Fig. 1 B), suggesting that F-actin is essential for cell–cell fusion. Consistent with the molecular function of the pheromone-dependent formin Fus1, F-actin did not accumulate at the site of fusion in *fus1Δ* pairs, though dynamic actin patches were detected at the shmoo tip of these cells (Fig. 1, C and D; Fig. S1; and Video 2). Similarly, *fus1*-dependent actin accumulation at the fusion site was previously observed on fixed cells and described as an accumulation of actin patches (Petersen et al., 1998a,b). In contrast, we describe in Figs. 2 and S2 a distinct architecture and composition of this actin structure, which we named the actin fusion focus.

Mutation or deletion of actin ring, patch, and cable components did not impair fusion focus formation. Indeed, F-actin accumulated at the fusion site during mating, and cell pairs fused even when actin cables were disrupted by *for3* deletion (Fig. S2, A and C). Similarly, *cdc12-112* mutants, or even *cdc12-112 for3Δ* double mutants, accumulated F-actin at the fusion site, mated, fused, and generated complete tetrads at 33°C both in homothallic crosses and in heterothallic crosses with wild-type cells (Fig. S2, D and E), a temperature at which these mutants fail to assemble a cytokinetic ring (Bendezú and Martin, 2011; Zhou et al., 2015). Thus, these other formins are not required for cell fusion. We could not completely disrupt actin patches, as endocytosis is required for earlier mating events, such as pheromone signaling and shmoo polarization (Iwaki et al., 2004). However, deletion of nonessential actin patch components involved in Arp2/3 activation (*dip1*Δ and *vrp1*Δ) did not prevent F-actin accumulation at the fusion site and only mildly affected fusion efficiency in heterothallic crosses with wild-type cells (Fig. S2, B and C). Thus, the fusion focus forms largely independently of the actin ring, actin patches, and actin cables.

We probed the polarity of actin filaments in the fusion focus by monitoring the localization of the barbed end–directed type V myosin motor Myo52 and the formin Fus1 (Fig. 2, A and B). Myo52-tdTomato formed a sharp dot at the fusion site (one in each partner cell; Fig. 3), which was located proximal to the shmoo tip and surrounded by F-actin on its cell-internal side (Figs. 2 A and S2 F). Fus1–superfolder

Downloaded from jcb.rupress.org on March 31, 2015

Published March 30, 2015

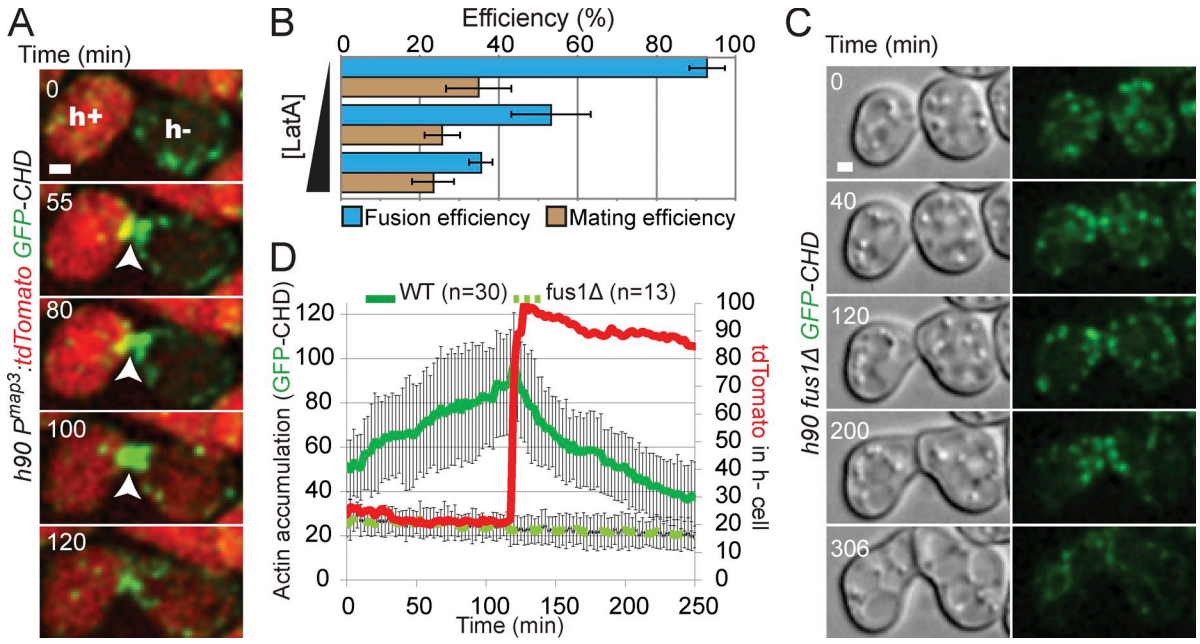

Figure 1. **Fus1-dependent actin accumulation at the prospective fusion site.** (A) Homothallic *h90 p^{map3}:tdTomato GFP-CHD* strain. Arrowheads show the fusion site where actin gradually accumulates. Fusion between partner cells occurs at 100 min as shown by appearance of the tdTomato signal in the *h*$^-$ cell. (B) LatA treatment reduces fusion efficiency of wild-type homothallic *h90* strain. Mating cells were starved in MSL−N for 4 h, to allow pheromone response and shmooing, before addition of increasing concentrations of LatA (0, 50, and 200 µg/µl). Cells were immediately spotted on MSL−N 2% agarose pads (not containing LatA and thus diluting the LatA concentration) and incubated overnight at 25°C before imaging for fusion efficiency quantification. $n > 200$. (C) Homothallic *h90 fus1Δ GFP-CHD* strain. Cells grow toward each other but are unable to fuse. Though actin patches are present, no actin focus is detected. (D) Quantification of GFP-CHD intensity at the zone of cell contact and of *p^{map3}*-driven tdTomato intensity in the *h*$^-$ partner cell in homothallic *h90* wild-type mating pairs expressing both markers (as in A). Individual curves were aligned to fusion time and averaged. GFP-CHD intensity at the zone of cell contact in *fus1Δ* is also indicated, though no alignment could be performed as a result of fusion failure. Error bars are standard deviations. WT, wild type. Bars, 1 µm.

GFP (sfGFP) colocalized with Myo52 at the fusion site as a concentrated dot before fusion and, like the fusion focus, disappeared after fusion (Fig. 2, B and C). Deletion of *fus1* disrupted Myo52 dot formation but not its localization at the shmoo tip (Fig. 2, D and E). These data suggest that the formin Fus1 and the type V myosin Myo52 mark a site of actin filaments assembly and focalization.

Time-lapse live-cell 3D structured illumination microscopy (SIM) indeed revealed long and short actin filaments, of mean length of 1.8 µm, emerging from the fusion focus in wild-type cells (Fig. 2, F and G; Fig. S2 F; and Video 3). In *for3Δ* cells, we still observed clear actin filaments, of reduced length (~0.7 µm), emanating from the focus (Fig. 2, F and G; and Video 4). In contrast, in *fus1Δ* cells, actin cables were significantly longer (~3 µm) and not focalized (Fig. 2, F and G; and Video 5). In *for3Δ fus1Δ* double mutants, no actin cables were observed. Similar observations were obtained by scanning confocal microscopy (Videos 7 and 8). This suggests that Fus1 and For3 assemble cables of distinct length and organization, with Fus1 assembling short, highly focalized cables and For3 assembling longer, more broadly distributed cables, as during mitotic growth (Feierbach and Chang, 2001). In both SIM and confocal time-lapse imaging, we also noted that actin patches often appeared to be moving toward the fusion site in *fus1*$^+$ cells (Videos 3–8). We conclude that the actin fusion focus is an aster of actin filaments, whose barbed ends are focalized at a single membrane-proximal region.

We further probed the actin-binding protein composition of the fusion focus. Like Myo52 and Fus1, the actin cable components tropomyosin Cdc8, calmodulin Cam2, and the second type V myosin Myo51, formed strong dots at the fusion site, consistent with previous description of their localization (Figs. 2 H and S2 G; Kurahashi et al., 2002; Itadani et al., 2006; Doyle et al., 2009). The ubiquitous F-actin binding protein coronin Crn1 also strongly accumulated at the fusion site, decorating the entire actin focus (Fig. S2 H). In contrast, the formin For3, responsible for actin cable formation, was present at the shmoo tip but did not form a tight dot and only very partially colocalized with Myo52 at the fusion site (Fig. 2 H). We also did not detect actin ring markers, such as the formin Cdc12, the FCH (Fes/CIP homology) protein Cdc15, or the myosin light chain Rlc1, at the fusion site (Figs. 2 H and S2 G). Finally, Arp2/3 complex components (Arc5), Arp2/3 activators (Wsp1 and Myo1), and other actin patch components (Dip1 and Cdc15) did not form a tight dot at the fusion site, though they were present at the shmoo tip over a broader area (Figs. 2 H and S2 G). Fig. 2 I provides a summary of the localization of all actin-binding factors investigated.

In summary, the actin fusion focus does not simply represent a local enrichment of actin patches but defines a distinct underlying actin structure. This structure resembles For3-nucleated actin cables in composition but is nucleated by the distinct formin Fus1 and is organized in an aster-like structure with actin filament barbed ends focalized at a membrane-proximal location.

Downloaded from jcb.rupress.org on March 31, 2015

Published March 30, 2015

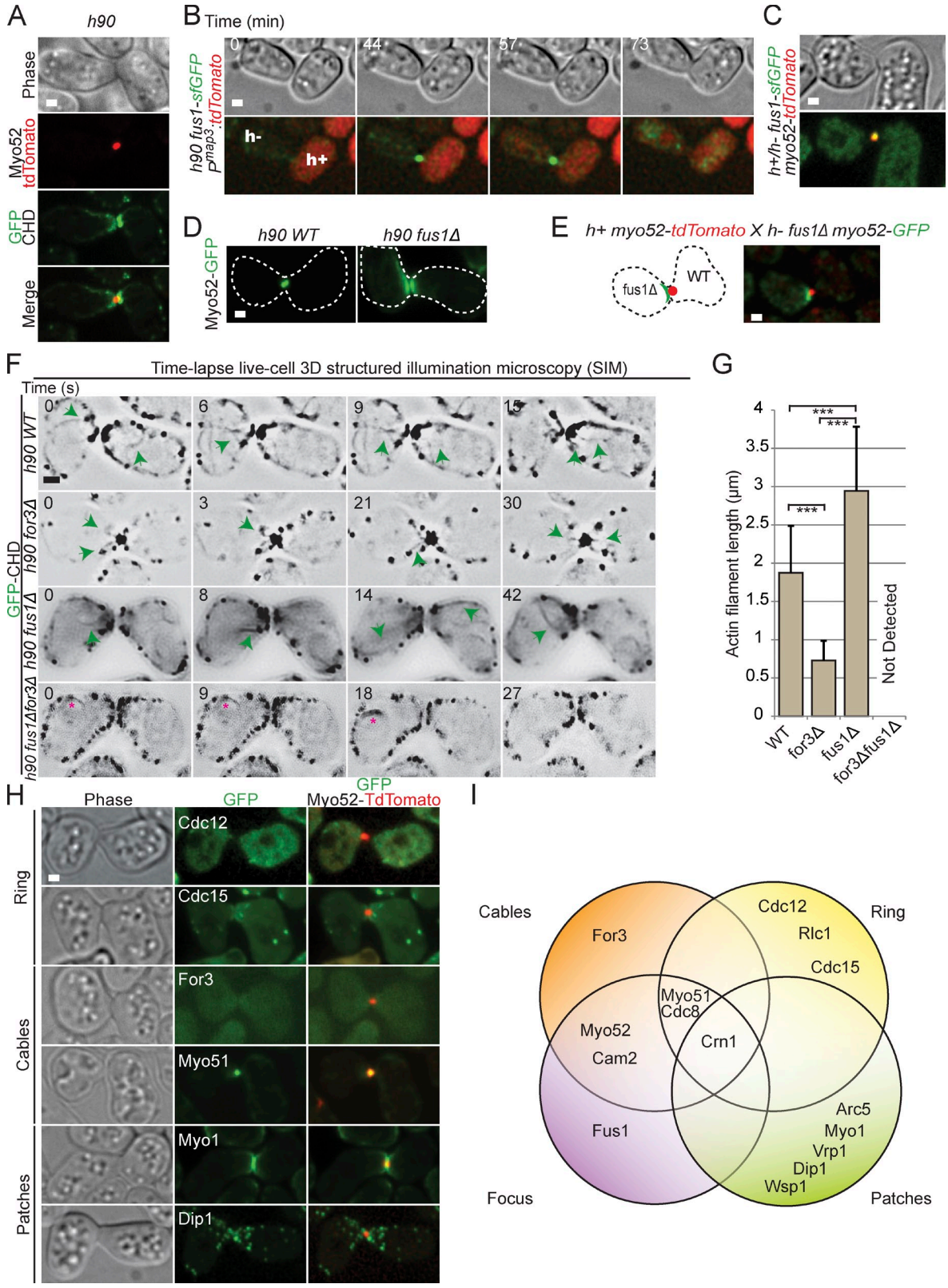

Figure 2. **Composition and architecture of the actin fusion focus.** (A) Homothallic *h90 myo52-tdTomato GFP-CHD* strain. Myo52 localizes as an intense dot at the cell–cell contact site, at the edge of the actin density. (B) Time-lapse imaging of homothallic *h90 fus1-sfGFP* p^{map3}*:tdTomato* strain. Entry of tdTomato in the h^- cell is used as a marker for fusion. Fus1 is detected as an intense dot at the cell–cell contact site. (C) Homothallic *h90 myo52-tdTomato fus1-sfGFP* strain. Myo52 and Fus1 colocalize at the fusion site. (D) Homothallic *h90* wild-type (left) and *fus1Δ* (right) strains expressing Myo52-GFP. Myo52 localizes as a crescent at the shmoo tip in the absence of Fus1. Cell outlines are shown with dotted lines. (E) Cross of heterothallic h^+ *myo52-tdTomato* and *h90 fus1Δ myo52-GFP*. Myo52 forms a crescent in the *fus1Δ* cell and a dot in the wild-type cell. (F) 3D SIM time-lapse of GFP-CHD in homothallic *h90* wild-type (WT), *for3Δ*, *fus1Δ*, and *fus1Δ for3Δ* mating pairs. Inverted images are shown. Green arrows point to actin filaments emanating from the fusion focus.

Downloaded from jcb.rupress.org on March 31, 2015

Published March 30, 2015

Analysis of Myo52 localization and dynamics reveals multiple steps in fusion focus formation

We studied the formation of the fusion focus by time-lapse microscopy of the entire mating process over several hours, using Myo52 as a marker. In early stages, Myo52 was detected as a pool of dots collectively forming a crescent at the shmoo tips of both partner cells. This crescent then compacted into a single focus in each cell, such that each mating pair showed two dots in close proximity at their contact site (Fig. 3 A; see model in Fig. 6 A). Over time, the distance between the two dots reduced, suggesting progressive degradation of the cell wall between the partner cells (Fig. 3, A and B). The distance between Myo52-tdTomato dots was measured relative to fusion time as defined by entry in the h^- cell of GFP driven by an h^+ cell-specific promoter (p^{map3}*:GFP*). After fusion, the Myo52 focus disassembled within 13.9 ± 4.5 min (n = 20). To measure the distance once the two dots were within the light diffraction limit, we used Myo52 tagged with distinct fluorophores in the two mating partners until focus disassembly. The time between apparent overlap of the two dots to disassembly was 20.7 ± 3.5 min (n = 20). By aligning the two curves on the time of focus disassembly, we conclude that the two Myo52 dots converge into an apparent single dot at the contact between the two cells ∼7 min before fusion pore opening (Fig. 3 B) and are disassembled ∼14 min after fusion.

Examination of Myo52-tdTomato or Myo52-GFP dynamics by FRAP in homothallic mating cells revealed that the crescent and dot localizations of Myo52 exhibit distinct dynamic turnover: Myo52-tdTomato was highly dynamic when it localized as a crescent at shmoo tips, displaying a FRAP half-time of ∼5 s. This indicates that half of the Myo52 molecules exchange in the crescent within 5 s. This was indistinguishable from its dynamics at cell tips in vegetative growing cells (Fig. 3 C). In contrast, Myo52 was significantly more stable when it was compacted in a dot during cell fusion, with FRAP half-time of ∼20 s (Fig. 3 C), suggesting Myo52 forms distinct or longer-lived molecular connections in the fusion focus than on actin cables. Consistent with the role of Fus1 in focalizing Myo52, this slower half-time in the dot was dependent on Fus1 (Fig. S3 A). No significant difference was detected in comparing Myo52 dynamics at the fusion focus when a dot was present in each partner cell or when a single unresolved dot was present at the interface of the two partners at the end of the process (Fig. 3 C).

To better understand the formation of the fusion focus, we centered our analysis on the transition between the Myo52 crescent and the focus, using high temporal resolution time-lapse microscopy acquiring images at a 1-s interval. We monitored Myo52-tdTomato localization in homothallic *h90* cells in which mating type was visualized by h^+ cell-specific GFP expression (p^{map3}*:GFP*; Fig. 3 D). Unexpectedly, the transition between the Myo52 crescent and the focus was asymmetric, with one cell forming an apparently stable Myo52 dot sooner than the other (Video 9). This asymmetry was highly predictable: in all cases (n > 50), the h^- cell exhibited a stable Myo52 dot before the h^+ cell, which exhibited a weaker, more fluctuating Myo52 signal, as shown in kymographs of the fusion site (Fig. 3 D). Myo52 dots were then stabilized in both cells before fusing into a single structure (Fig. 3 D). Measures of Myo52 dynamics further revealed asymmetries between the two mating types: first, the instantaneous displacement of Myo52-tdTomato between consecutive time points at 7.2-min intervals throughout the fusion process was significantly smaller in the h^- than the h^+ cell (Fig. 3, E and F). Second, FRAP analysis revealed that Myo52 recovery half-time in the fusion focus was significantly higher in h^- than h^+ cells (Fig. 3 G). Thus, the stabilization of the fusion focus is asymmetric and occurs in the h^- cell before the h^+ cell (see Fig. 6 A).

Remarkably, the localization of both the second Myosin V Myo51 and the formin Fus1 were also asymmetric between h^- and h^+ cells. When Myo52-tdTomato localized as a crescent at the beginning of the fusion process, Myo51-3YFP and Fus1-sfGFP signals were very low or undetectable (Fig. 3, H and I; and Fig. S3 B). Myo51 accumulated at the fusion site concomitant with the stabilization of Myo52 into a dot first in the h^- cell and later in the h^+ cell, with the h^- cell type identified as the cell with a stable Myo52 dot (Figs. 3 H and S3 B and Video 9). Myo52 and Myo51 then colocalized perfectly until fusion, though the Myo51-3YFP signal disappeared first during fusion (Fig. 3 H). Like Myo52, Myo51 localization to a dot required Fus1 (Fig. S3 C). Similarly, Fus1 distribution was asymmetric, with only the h^- cell, with a strong Myo52 dot showing a clear colocalization with Fus1, whereas the h^+ cell with a more dispersed and less intense Myo52 localization showed no or very weak Fus1 signal (Fig. 3 I). This asymmetry was not present in later stages of fusion when Myo52 and Fus1 colocalized in both cells. In conclusion, the localization and dynamic behavior of myosin V and formin Fus1 reveal a stepwise, asymmetric maturation of the cytoskeletal structure that underlies cell fusion.

Type V myosins Myo52 and Myo51 are crucial for cell–cell fusion

We tested the function of type V myosins during cell fusion. Myosin V deletion strains (*myo51Δ* and *myo52Δ* and the double *myo51Δmyo52Δ* mutant, noted *myoVΔ* throughout) fused inefficiently with wild-type cells and were fusion defective when

No actin cables were detected in *fus1Δ for3Δ* double mutant, but some mating pairs showed a perinuclear actin ring (asterisks). (G) Mean length of actin filaments emanating from the fusion focus in strains as in F. Filaments are significantly shorter in *for3Δ* and longer in *fus1Δ* than wild-type cells (*t* test, ***, P < 10^{-6}). This indicates that Fus1-dependent filaments are shorter than For3-dependent filaments and that wild-type cells likely contain both types. n = 30 actin filaments measured in three distinct mating pairs. Error bars are standard deviations. (H) Crosses of heterothallic h^+ and h^- *myo52-tdTomato* strains coexpressing Cdc12-3GFP, mEGFP-Cdc15, For3-3GFP, Myo51-3YFP, mGFP-Myo1, or Dip1-GFP. Images shown are time-averaged maximum intensity projection of 15 z stacks over 15 min. (I) Venn diagram summarizing the actin binding proteins that we show to be localized or not at the actin fusion focus. Attribution to cables, ring, or patches is adapted from Kovar et al. (2011). Bars, 1 µm.

Downloaded from jcb.rupress.org on March 31, 2015

Published March 30, 2015

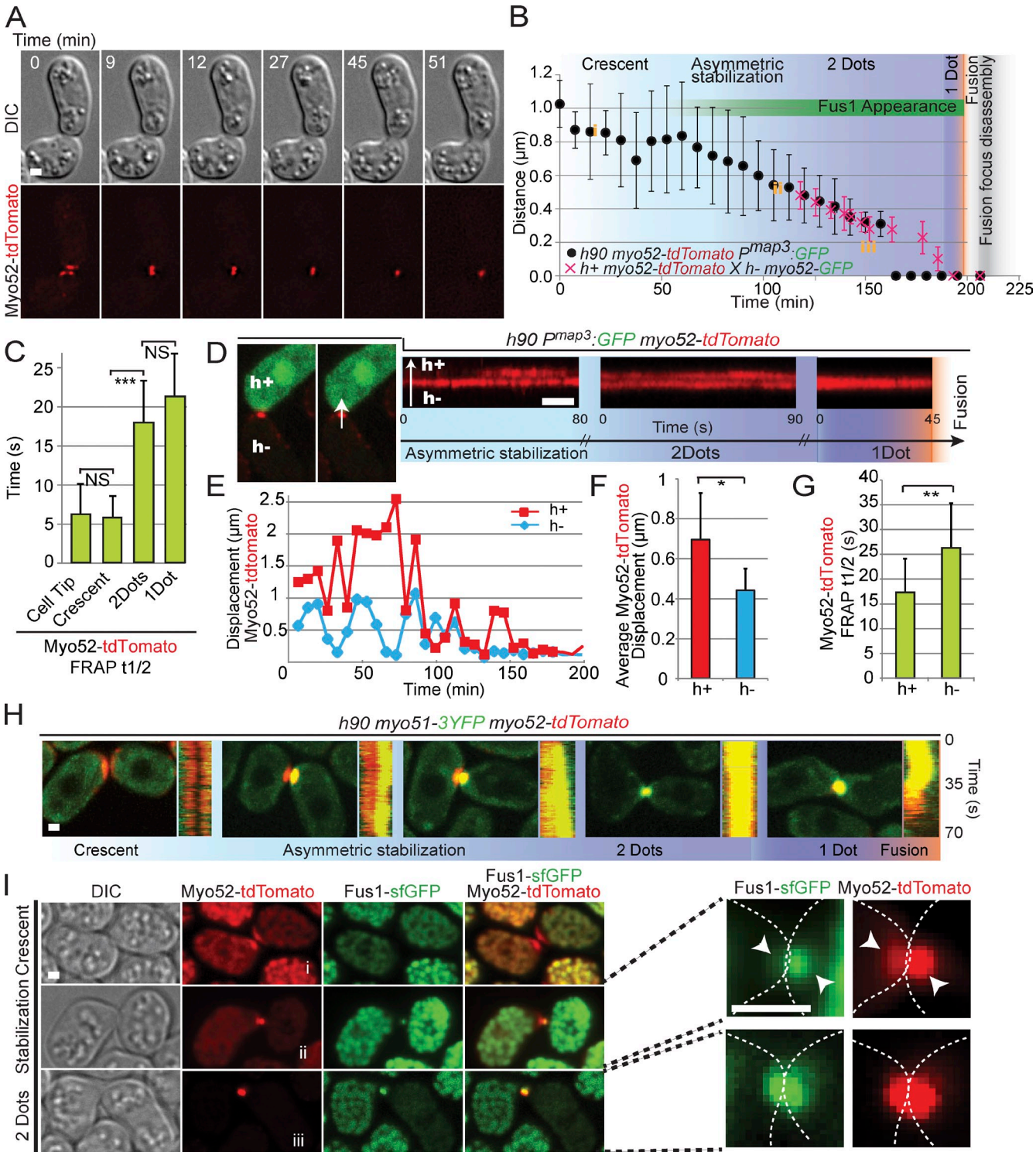

Figure 3. **Type V myosin localization and dynamics define multiple steps in the formation of the fusion focus.** (A) Time-lapse images of homothallic *h90 myo52-tdTomato* strain. (B) Distance between Myo52 signals in the two partner cells. The black symbols show mean distances over time in *h90 myo52-tdTomato* P^{map3}*:GFP* cell pairs ($n = 20$), aligned to fusion time. The red symbols show mean distances over time in h^+ *myo52-tdTomato* × h^- *myo52-GFP* ($n = 20$), aligned to the time of fusion focus disassembly. The two curves were then manually aligned to the time of fusion focus disassembly. The distinct phases of Myo52 localization as described in the rest of the figure are indicated; i.e., the crescent phase, the asymmetric dot stabilization phase, the two-dot phase, and the one-dot phase. Note that the one-dot phase simply indicates that two dots cannot be resolved. The length of the asymmetric phase, during which a dot is observed in the h^- cell, whereas a crescent or a mobile dot is present in the h^+ cell, is variable from pair to pair. The yellow i, ii, and iii refer to the distances between Myo52 structures measured in I and thus provide an indication of the timing of Fus1 appearance. (C) Mean FRAP recovery half-times of Myo52-tdTomato at the cell tip of vegetative growing cells or at indicated steps of cell–cell fusion. Homothallic *h90* pairs expressing Myo52-tdTomato and Myo51-3YFP were used for this experiment to precisely monitor the appearance of the stable two-dot phase (see H). Cells with distinct, focalized Myo51 signals were attributed to the two-dot and one-dot categories. Myo52 is less mobile when localized at the fusion focus. *t* test, ***, $P = 1.9 \times 10^{-7}$; $n = 15$ for each category. (D) High-temporal resolution imaging of homothallic *h90 myo52-tdTomato* p^{map3}*:GFP* strain. The h^+ cell-specific GFP expression allows

Downloaded from jcb.rupress.org on March 31, 2015

Published March 30, 2015

crossed to *fus1Δ* (Fig. 4 A). We note that *myoVΔ* cells fused more efficiently with h^+ than h^- wild-type partners (not depicted), as also observed for *fus1Δ* × wild type (Fig. 4, compare A and H), though the significance of this observation is currently unknown. Homothallic *myoVΔ* cells were also fusion defective. However, even *myoVΔ* double mutant displayed efficient mating pair formation (similar to their ability to polarize during mitotic growth; Motegi et al., 2001; Win et al., 2001; Bendezú and Martin, 2011), suggesting the observed fusion defect is not caused by prior cell polarization defects. The stronger phenotype of the *myoVΔ* double mutant, compared with each single mutant, indicates that Myo51 and Myo52 contribute at least partially overlapping function to cell fusion. Fus1 displayed a broader localization in myosin V mutants, especially in the double mutant in which it localized over the entire surface at the contact zone (Fig. 4, B and C). Similarly, actin accumulation at the fusion site spread along the contact zone in the double *myoVΔ* mutant (Fig. 4 D). Thus, type V myosins are required for focalization of the formin Fus1 and of actin filaments in the focus. As we have shown in Fig. 2 (D and E) that Fus1 is required for myosin V focalization, we conclude that actin fusion focus formation relies on positive reinforcement between formin and type V myosins.

Although Myo51 and Myo52 are together essential to achieve cell fusion, we note that each single mutant displayed a distinct phenotype after fusion. Tetrads derived from homothallic *h90 myo52Δ* mating reactions often displayed residual undigested cell wall at the fusion site (Fig. 4, E and F), suggesting defective cell wall degradation during cell fusion. In contrast, tetrads derived from *h90 myo51Δ* mating reactions showed a narrower neck compared with wild type, suggesting a defect in neck expansion after fusion (Fig. 4, E and F). Thus, in addition to their functional overlap for cell–cell fusion, each type V myosin may have distinct roles in postfusion events.

Most type V myosins serve to transport cargoes through interaction with their C-terminal tail. We investigated the effect of deleting the cargo-binding C-terminal tail domain of type V myosins on cell–cell fusion. Both Myo52$^{\Delta tail}$-tdTomato and Myo51$^{\Delta tail}$-3YFP localized as a dot at the fusion site, indicating that their cargo-binding domain is not essential for fusion focus formation (Fig. 4 G). Interestingly, cell fusion was impaired in *myo52$^{\Delta tail}$* mutants, whereas *myo51$^{\Delta tail}$* mutants remained fusion competent in crosses to *fus1Δ* partner cells (Fig. 4 H). These results are similar to observations made on the function of type V myosin in actin cable organization during vegetative growth (Lo Presti et al., 2012). They suggest that Myo52 promotes cell fusion by delivering cargoes, whereas Myo51 may play a more structural, C-terminal tail-independent role for fusion focus formation.

Type V myosins deliver cell wall degradation enzymes for cell fusion

Cell fusion in yeast requires important cell wall remodeling, to allow plasma membrane contact while preserving cell integrity. The progressive shortening of the distance between Myo52 dots during fusion suggests that the cell wall may be progressively eroded. We thus tested whether the fusion focus is required to localize cell wall degrading enzymes. We used GFP tagged alleles of seven distinct glucanases—the endo-α(1,3)-glucanases Agn1 and Agn2 (Dekker et al., 2004, 2007), the endo-β(1,3)-glucanases Eng1 and Eng2 (Martín-Cuadrado et al., 2003, 2008), and the β(1,6)-glucanases Exg1, Exg2, and Exg3 (Dueñas-Santero et al., 2010). Remarkably, all seven colocalized with Myo52-tdTomato at the fusion focus (Fig. 5 A). Deletion of each single one of these, except *eng1Δ*, led to reduction in fusion efficiency in crosses to *fus1Δ* (Fig. 5 B). Examination of mating pairs that failed to fuse revealed cell wall at the cell–cell junction, as for *fus1Δ* and *myoVΔ* pairs, suggesting the cell wall is not degraded (Fig. 5 C). We also observed a high occurrence of cell lysis, suggesting deregulation of the fusion process (unpublished data). Further combinatorial double and triple deletion of *agn2*, *eng2*, and *exg3* led to progressive decrease in fusion efficiency, indicating that each glucanase additively contributes to fusion.

In contrast to the focalized localization of glucanases, the cell wall β(1,3)-glucan synthases Bgs1 and Bgs4 (Cortés et al., 2002, 2005) decorated the entire shmoo tip (Fig. 5 D). Thus, during cell–cell fusion, cell wall glucanases are focalized at the fusion focus within a broader zone of cell wall synthases.

Finally, we studied the dependency of glucanases on fusion focus formation by tagging one member from each family—Agn2, Eng2, and Exg3—with sfGFP, which we found provides significantly stronger signal for many tagged proteins, likely because of its faster maturation time (Fig. 5 E; Pédelacq et al., 2006). In *fus1Δ*, the glucanases decorated the entire shmoo tip, similar to Myo52. In *myoVΔ*, they failed to localize to either shmoo tip or fusion focus, suggesting they may be cargoes for the type V myosins (Fig. 5 F). In agreement with this idea, the glucanases failed to localize to the fusion focus

to mark the two cell types. The left images show a pair with a stable focus only in the h^- cell. The right images show kymographs of Myo52-tdTomato at the fusion site in different h^- and h^+ partner cells at distinct stages of the fusion process: during asymmetric dot stabilization, when a stable dot is present in each cell, and after the two dots have merged into one. In early stages, Myo52-tdTomato is more stable in the h^- cell than the h^+ cell. The arrow represents the direction of the line drawn to make the kymographs. (E) Instantaneous displacement of Myo52-tdTomato signal over the entire fusion process. The graph shows one representative mating pair. (F) Mean Myo52-tdTomato instantaneous displacement over the entire mating process (n = 8 cells). *t* test, *, $P = 1.8 \times 10^{-2}$. (G) Mean FRAP recovery half-times of Myo52-tdTomato focus in heterothallic h^- (n = 10) or h^+ (n = 12) *myo52-tdTomato* mating cells crossed to cells expressing CHD-GFP. *t* test, **, $P = 8.19 \times 10^{-3}$ (H) Time-averaged projections and kymographs of *h90 myo52-tdTomato myo51-3YFP* cells, imaged every second over 70 s. Myo51 strongly colocalizes with Myo52 upon asymmetric dot stabilization. (I) Time-averaged projections over 2 min of *h90 myo52-tdTomato fus1-sfGFP* mating, imaged every 30 s. Mating pairs at crescent, asymmetric dot stabilization and two-dot stages are shown. i, ii, and iii refer to distance between dots, as highlighted in B. Right images show enlargements of the fusion site. Arrowheads point out the difference in intensity of Myo52-tdTomato and Fus1-sfGFP between both mating partners. Dotted lines show the outline of the mating pair. DIC, differential interference contrast. Bars, 1 µm. Error bars are standard deviations.

Downloaded from jcb.rupress.org on March 31, 2015

Published March 30, 2015

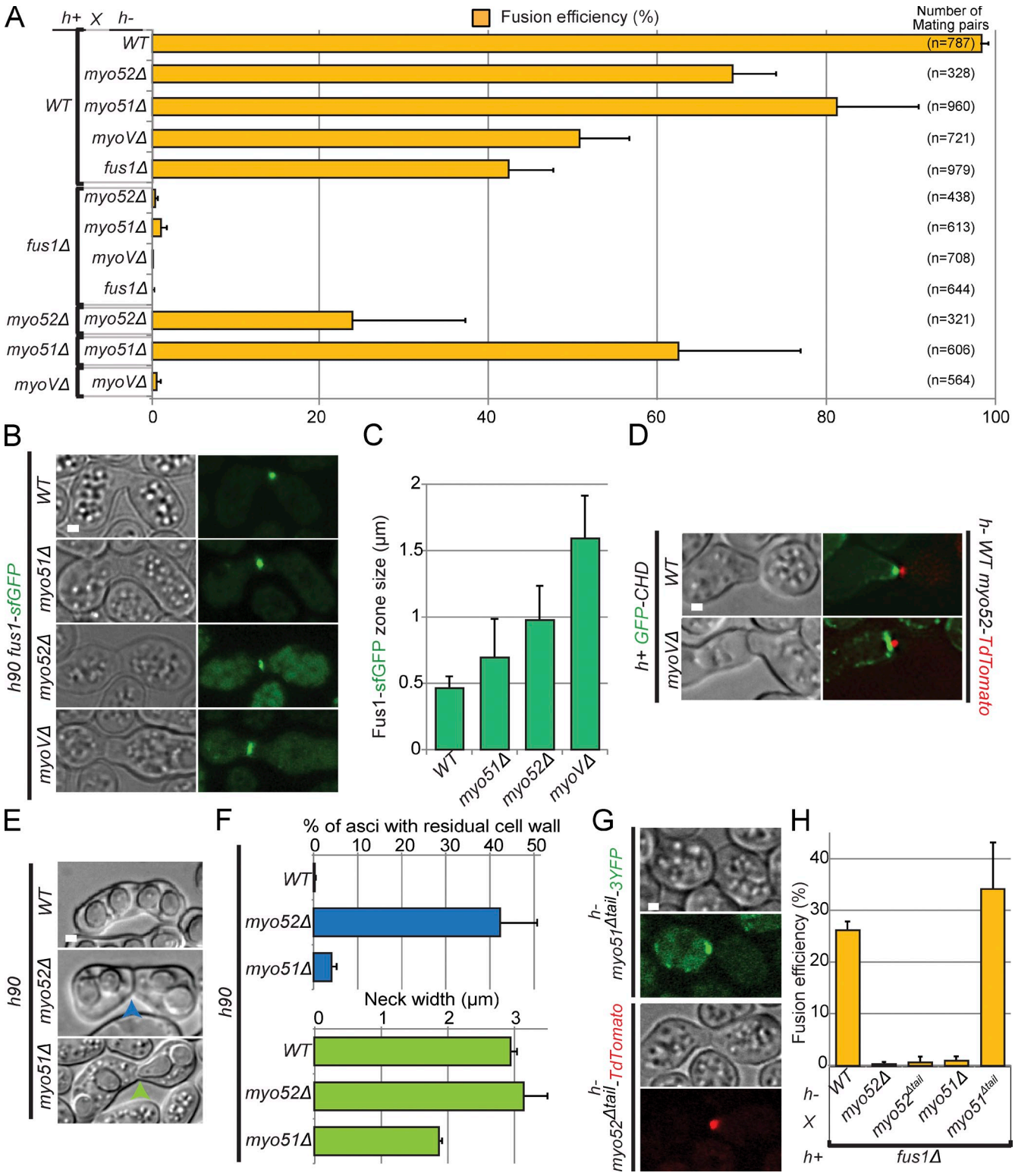

Figure 4. **Type V myosins Myo52 and Myo51 are essential for cell fusion.** (A) Fusion efficiency of indicated heterothallic crosses. *myoVΔ* (=*myo51Δ myo52Δ* double mutant) is unable to fuse with either *fus1Δ* or itself. The total number of mating pairs analyzed (three experiments combined) is indicated on the right. (B) Homothallic *h90* wild-type, *myo51Δ*, *myo52Δ*, and *myoVΔ* strains expressing Fus1-sfGFP. Images are time-averaged projections over time 15 min at 1 image/min. Type V myosins are important for Fus1 focalization. (C) Quantifications of Fus1-sfGFP zone size in strains as in B; $n = 12$. (D) Crosses of h^+ *wild-type* (*WT*) and *myoVΔ* strains expressing GFP-CHD to h^- *myo52-tdTomato*. Images are time-averaged projections over 15 min at 1 image/min. Type V myosins are important for actin focalization at the fusion site. (E) Asci derived from homothallic *h90 myo52Δ* and *myo51Δ* matings. We observed residual cell wall (blue arrowhead) and narrow necks (green arrowhead) in *myo52Δ* and *myo51Δ*, respectively. (F) Percentage of asci with residual cell wall and mean neck width in strains as in E. $n > 200$. (G) Crosses of h^- *myo51*$^{\Delta tail}$*-3YFP* (top) and h^- *myo52*$^{\Delta tail}$*-tdTomato* (bottom) to h^+ *wild-type* cells. Both truncated motors localize correctly to the fusion focus. (H) Fusion efficiency of indicated heterothallic crosses. Note that a lower fusion efficiency is observed for h^+ *fus1Δ* × h^- *wild type* than for h^- *fus1Δ* × *h+ wild type* in A. $n > 100$. Bars, 1 μm. Error bars are standard deviations.

Downloaded from jcb.rupress.org on March 31, 2015

Published March 30, 2015

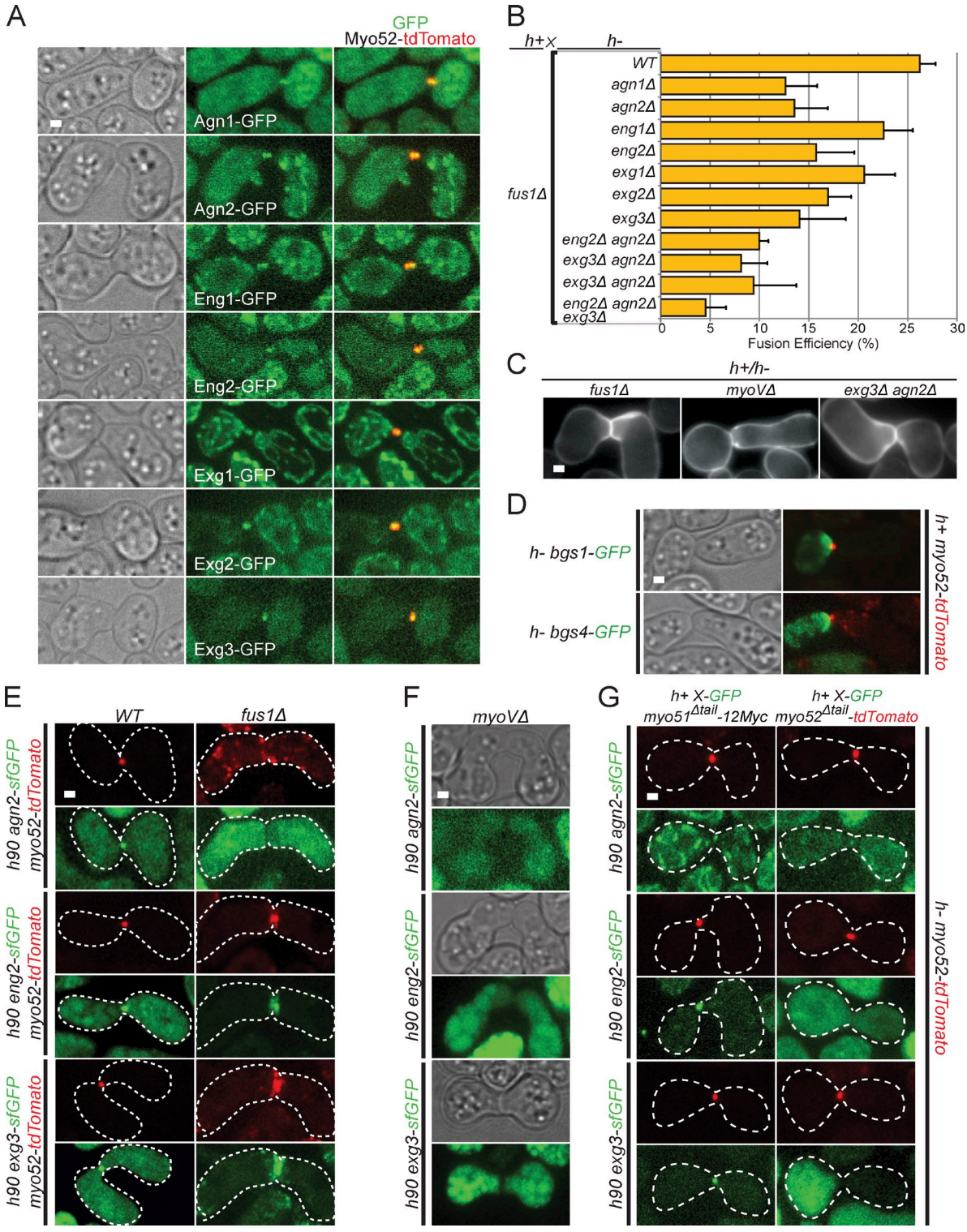

Figure 5. **Cell wall degradation enzymes focalize at the fusion focus.** (A) Crosses of heterothallic h^- and h^+ *myo52-tdTomato* strains expressing GFP-tagged glucanases as indicated. All glucanases localize to the fusion focus. (B) Fusion efficiency of crosses between h^+ *fus1Δ* strains and h^- single, double, and triple glucanase deletion strains. $n > 100$. (C) Calcofluor images of nonfusing pairs in heterothallic crosses of h^+ *fus1Δ*, *myoVΔ*, and *agn2Δ eng2Δ* to h^- *fus1Δ*, *myoVΔ*, and *agn2Δ eng2Δ*, as indicated. This shows presence of cell wall at the cell–cell contact. (D) Time-averaged projections over 10 s of crosses of heterothallic h^- *bgs1-GFP* (top) and *bgs4-GFP* (bottom) to h^+ *myo52-tdTomato*, imaged every second. Cell wall synthases localize as a crescent at the fusion site. (E) Homothallic *h90 wild type* (left) and *fus1Δ* (right) *myo52-tdTomato* strains coexpressing sfGFP-tagged versions of Agn2, Eng2, and Exg3. Cell wall glucanases colocalize at fusion site with Myo52 either as a dot in *wild type* or as a crescent in fusion-deficient *fus1Δ* cells. Cell outlines are shown with dotted lines. (F) Homothallic *h90 myo51Δ myo52Δ* (*myoVΔ*) strains coexpressing sfGFP-tagged versions of Agn2, Eng2, and Exg3. Glucanases are not detected at fusion site. (G) Heterothallic h^+ *myo51*$^{\Delta tail}$*-12Myc* (left) and h^+ *myo52*$^{\Delta tail}$*-tdTomato* (right) strains coexpressing sfGFP-tagged versions of Agn2, Eng2, and Exg3 crossed to h^- *myo52-tdTomato* cells. Cell wall glucanases localize at the fusion site in *myo51*$^{\Delta tail}$ mutants but not, or are highly reduced, in *myo52*$^{\Delta tail}$. WT, wild type. Error bars are standard deviations. Cell outlines are shown with dotted lines. Bars, 1 µm.

Downloaded from jcb.rupress.org on March 31, 2015

Published March 30, 2015

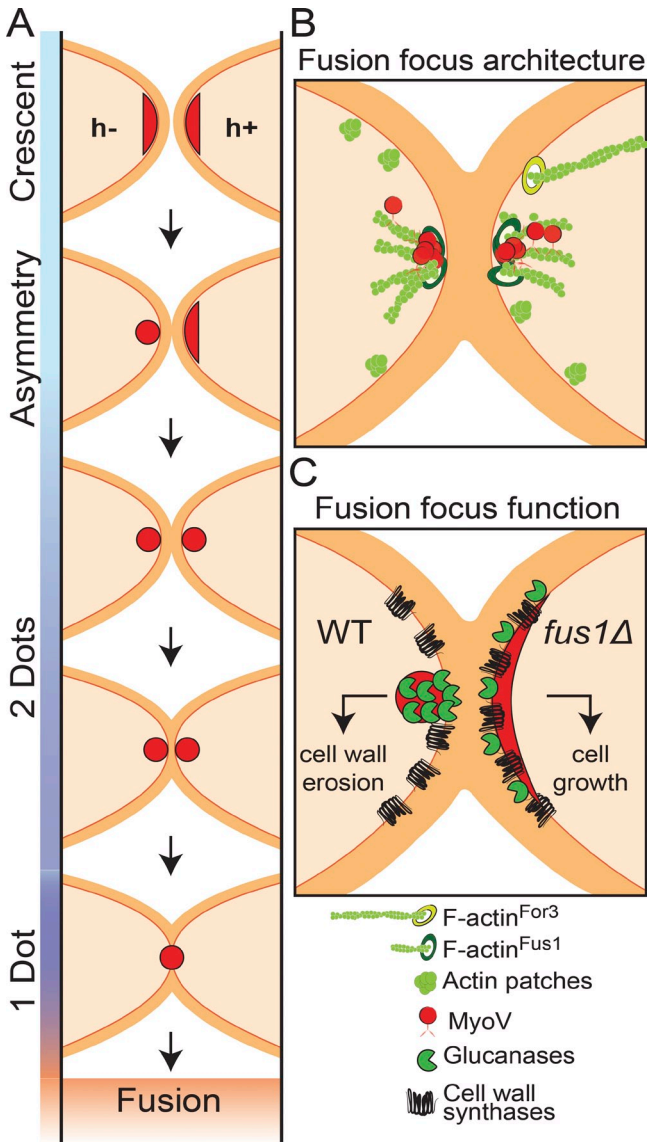

Figure 6. **Model for the fusion focus multi-step formation, architecture, and function.** (A) Schematic representation of the cell–cell fusion process in fission yeast. Type V myosins first assume a crescent localization, decorating the shmoo tip. Focalization is observed in the h^- cell fist and then in the h^+ cell. The distance between the two dots then reduces over time, indicating cell wall thinning, until the two structures merge into one and fusion occurs. (B) Illustration of the architecture of the fusion focus. The formin Fus1 nucleates short actin filaments, which are focalized with type V myosins near the plasma membrane. Focalization requires both Fus1 and type V myosins. Longer For3-nucleated cables are also polarized toward the shmoo tip. (C) Model of the function of the fusion focus. For comparison, the wild-type situation is compared with that in *fus1Δ* cells. In the wild type, glucanases are concentrated at the fusion focus, therefore segregating them from the location of cell wall synthases, which decorate the entire shmoo tip. This geometrical organization permits cell wall thinning and fusion. In absence of Fus1, the localizations of glucanases and cell wall synthases overlap over the shmoo tip, promoting cell growth.

in $myo52^{\Delta tail}$ mutant cells, which show fusion defect but form a fusion focus. In contrast, they localized correctly in $myo51^{\Delta tail}$ mutants, which do not exhibit fusion defects (Fig. 5 G). In conclusion, glucanases are cargoes for myosin V Myo52, which concentrates them at the fusion focus for cell wall digestion during cell fusion.

Discussion

Architecture of the fusion focus

We present here a novel actin structure in yeast, the actin fusion focus. The fusion focus is assembled by the formin Fus1, which has long been known to underlie cell–cell fusion (Petersen et al., 1995). Fus1, like other formins, nucleates linear actin filaments (Scott et al., 2011). However, the specific actin structure it organizes was not understood.

The fusion focus is distinct from actin patches, organized by the Arp2/3 actin nucleator. Most actin patch components do not assume a tight localization at the fusion site, and Arp2/3 activators are not strongly involved in cell–cell fusion, consistent with data in the budding yeast that many endocytosis mutants do not have a fusion defect (Brizzio et al., 1998). We note that earlier requirements of endocytosis for pheromone signaling and polarized growth preclude complete inactivation of the Arp2/3 complex and that a function of Arp2/3 and endocytosis in cell–cell fusion can therefore not be excluded. Indeed, the apparent directional movement of actin patches toward the fusion site seen in our high-resolution time-lapse imaging suggests they may for instance contribute to membrane recycling. However, our data demonstrate that, although actin patches normally accumulate in the vicinity of the prospective fusion site (Petersen et al., 1998a), they are superimposed upon a distinct underlying actin structure.

The architecture of the fusion focus is also distinct from that of actin cables and the cytokinetic ring, nucleated by the two other formins For3 and Cdc12. Actin cables are bundles of largely parallel actin filaments (Kamasaki et al., 2005), whereas the cytokinetic ring relies on an antiparallel actin filament organization (Kamasaki et al., 2007). In contrast, in the fusion focus, the focal localization of Fus1 and type V myosins at the edge of an actin cloud suggests an aster-like filament configuration centered round filament barbed ends. Structured illumination and confocal microscopy further support this architecture through observation of actin filaments emanating from the fusion focus. Thus, the actin fusion focus consists of an aster of actin filaments nucleated by the formin Fus1 (Fig. 6 B).

Formin Fus1 and type V myosins are required to form the fusion focus

The convergence of actin filaments in the fusion focus relies on both Fus1 and type V myosins, and these factors are codependent for focalization, suggesting positive reinforcement between Myosin V and formin Fus1. The role of type V myosins in formation of the fusion focus is reminiscent of the function of microtubule minus end-directed motors for spindle pole formation (Heald et al., 1997; Goshima et al., 2005). Here, multimerization of motor proteins is sufficient to form microtubule asters in vitro (Surrey et al., 2001). Minus end–directed motors, such as Dynein, also contribute to focalization by transporting kinetochore fibers along astral microtubules (Maiato et al., 2004). Myo51 and Myo52 may use similar mechanisms, for instance forming multimeric assemblies by interacting with vesicular cargoes and thus contributing to actin filament focalization. These motors may also more directly

Downloaded from jcb.rupress.org on March 31, 2015

Published March 30, 2015

transport Fus1, thus promoting new filament nucleation in the vicinity of existing barbed ends. In an analogous manner, we had previously shown that Myo52 associates with the formin For3 and contributes to its delivery to cell tips (Lo Presti et al., 2012). Our data showing distinct C-terminal tail requirements and postfusion phenotypes suggest that Myo51 and Myo52 each contribute to actin focalization through distinct mechanism. Distinct contributions of Myo51 and Myo52 were also previously observed in the organization and function of actin cables and the cytokinetic ring (Lo Presti et al., 2012; Wang et al., 2014). The role of type V myosins in focus formation is also reminiscent to that of Myosin X, a distinct myosin that promotes actin filament convergence for filopodia formation (Tokuo et al., 2007).

Fus1 is a key determinant of the fusion focus, though other actin-binding proteins, such as tropomyosin Cdc8, or profilin Cdc3, are likely also required (Petersen et al., 1998a; Kurahashi et al., 2002). Fus1 N-terminal FH3 domain confers localization to the shmoo tip (Petersen et al., 1998b), but it is unclear whether this domain alone promotes focalization. Interestingly, in vitro dissection of Fus1 FH1-FH2 domains revealed a unique set of activities, including actin filament nucleation, barbed end capping, elongation, and also bundling (Scott et al., 2011). What specific features of Fus1 confer its unique ability to organize the fusion focus remains to be tested.

Function of the fusion focus: Focalized delivery of cell wall–degrading enzymes

In walled cells under strong turgor pressure, such as those of fungi, cell–cell fusion requires precise remodeling of the cell wall to allow plasma membrane contact while protecting the cells from lysis: the cell wall has to be digested at precisely opposed locations in the two partner cells while maintained intact, likely reinforced, in surrounding regions. The fusion focus serves to precisely position and focalize the cell wall degradation machinery to permit this remodeling.

Indeed, we show that many, if not all, fission yeast glucanases are enriched at the fusion focus and required for efficient cell fusion. The yeast cell wall mainly consists of polymers of α- and β-glucans (Pérez and Ribas, 2004). The fusion focus–localized glucanases exhibit distinct hydrolytic activities, hydrolyzing the major linkage bonds in the glucan polymers. Focusing on three of these glucanases, Agn2, Eng2, and Exg3, we show they are likely cargoes of Myo52. Indeed, each of them fails to localize to the fusion focus in the *myo52*$^{\Delta tail}$ mutant, in which the cargo-binding tail of Myo52 is absent, yet the fusion focus forms correctly. Although many glucanases are either secreted or transmembrane proteins, and thus likely transported to the fusion site in secretory vesicles, one intriguing observation is that Agn2, Eng2, and Exg3 all lack a signal sequence or transmembrane domain (Dekker et al., 2004; Encinar del Dedo et al., 2009; Dueñas-Santero et al., 2010). Yet, in combination, these glucanases significantly contribute to fusion efficiency. How these proteins are delivered to the cell outside is currently unknown. In summary, these data show that the fusion focus concentrates these and other glucanases to a single location to promote cell wall erosion.

In contrast, the cell wall synthases Bgs1 and Bgs4 do not concentrate at the fusion focus but rather decorate the entire shmoo tip throughout the fusion process (Cortés et al., 2002, 2005). Bgs1 was proposed to be a Myo52 cargo (Mulvihill et al., 2006), but its localization in a broad crescent when Myo52 is focalized indicates that transport along actin filaments is not the sole determinant of its localization. Cell wall synthases may be delivered at the fusion focus but spread laterally from the zone of insertion, thus decorating the entire shmoo tip. This is in agreement with the observation that Bgs4 remains well polarized upon acute F-actin disruption (Cortés et al., 2005) or in the absence of directional transport along actin filaments (Bendezú and Martin, 2011), suggesting a long residence time at the polarized zone. Thus, the formation of the fusion focus creates a geometrical difference in the localization of cell wall synthases and hydrolases.

Two pieces of evidence indicate that focalization of the glucanases, rather than their mere localization to the shmoo tip, is required for fusion. First, the progressive thinning of the connecting cell wall, shown through reduction in distance between MyoV signals, occurs only after fusion focus formation. Second, the phenotype of *fus1Δ* cells shows that an unfocused localization of glucanases to the shmoo tip is not sufficient to promote cell fusion. Instead, *fus1Δ* cells keep growing toward each other, extending long projections (Petersen et al., 1995). These observations suggest that a change in the geometry of cell wall enzyme delivery distinguishes cell growth from cell fusion (or lysis if deregulated). Though changes in enzyme activities are also possible, this simple model does not need to invoke such changes. We propose that an overlapping distribution of cell wall synthases and hydrolases, as in *fus1Δ*, balances cell wall stretching and integrity for turgor pressure to drive polarized growth, as proposed for other tip-growing cells (Rojas et al., 2011). In contrast, specific focalization of the hydrolases within a broader distribution of the synthases may promote local cell wall thinning for fusion (Fig. 6 C).

Asymmetry in the cell fusion process

Fusion focus formation occurs asynchronously in the two cell types and is highly stereotypical, with the h^- cell always displaying a stable focus before the h^+ cell (Fig. 6 A). Thus, this asymmetry is caused by intrinsic differences between the two cell types. This may be a result of the slightly distinct sexual gene expression programs in the two types, though the number of mating type–specific factors identified is small (Mata and Bähler, 2006; Xue-Franzén et al., 2006). This may also be caused by distinct qualities of the two pheromones inducing temporally or spatially distinct responses in their partner cell. Indeed, previous data suggested that high local pheromone concentrations are needed for cell–cell fusion in the budding yeast (Brizzio et al., 1996). In either case, the delayed stabilization of the h^+ cell fusion focus always occurs at a site precisely facing the fusion focus of the h^- cell, suggestive of strong spatial communication between the two partner cells.

An important question is whether this asymmetry is physiologically important. The normally delayed formation of the fusion focus in the h^+ cell does not strictly depend on fusion competency

Downloaded from jcb.rupress.org on March 31, 2015

Published March 30, 2015

of the h^- cell. Indeed, cell fusion happens, though at reduced efficiency, in crosses between *fus1Δ* and wild-type cells irrespective of which partner is mutant, and is completely blocked only when both partners are mutant (Petersen et al., 1995). We made similar observations in *myoVΔ* mutants. We note however that fusion consistently occurs more readily in crosses of mutant cells with wild-type h^+ cells than h^- cells. We postulate that an asymmetric setup promotes precision in positioning of the two fusion machineries, ensuring formation of a single membrane contact site.

Parallels with cell–cell fusion events in other cells

The involvement of actin in cell–cell fusion is not unique to the fission yeast. In the budding yeast *S. cerevisiae*, although there is no cell fusion-specific formin, the actin cytoskeleton plays a critical role in the clustering of signaling and fusion molecules at the shmoo tip (Ayscough and Drubin, 1998; Bagnat and Simons, 2002). In addition, the formin Bni1 and the tropomyosin Tpm1 are required not only for shmoo polarization but also for cell fusion (Liu and Bretscher, 1992; Dorer et al., 1997); electron microscopy analysis described highly clustered vesicles over a small region (Gammie et al., 1998); and the fusion factor Fus2 focalizes in a polarizome-dependent manner at the fusion site (Paterson et al., 2008). Thus, although recent work proposed that local concentration of glucanases required for fusion stems from restricted diffusion upon cell–cell contact (Huberman and Murray, 2014), all these data are highly suggestive of the existence of a similar actin fusion focus in this organism to focalize the delivery of cell wall glucanases.

In nonwalled cells, fusion-specific actin structures also underlie cell fusion. A possible Formin3-dependent F-actin structure underlies tracheal cell fusion in *Drosophila melanogaster* (Tanaka et al., 2004), but the best-studied case occurs during myoblast fusion, in which the two fusing cells—a founder cell and a fusion-competent myoblast—organize an Arp2/3-dependent structure at the fusion site before fusion (Kim et al., 2007; Massarwa et al., 2007; Richardson et al., 2007; Sens et al., 2010). This structure is highly asymmetric, forming a fusion focus only in the fusion-competent myoblast, and likely provides force for fusion within an invasive podosome-like structure (Sens et al., 2010; Shilagardi et al., 2013). As podosomes are sites of extracellular matrix degradation (Linder, 2007), it suggests an interesting analogy with the role of the fusion focus in fission yeast. This analogy also raises the question of whether the Fus1-nucleated fusion focus in yeast provides force for fusion. Future work should reveal whether actin fusion foci of distinct molecular composition have evolved to fulfill the same tasks in diverse species.

Materials and methods

Strains, media, and growth conditions

Strains used in this study are listed in Table S1. Homothallic (*h90*) strains able to switch mating type or 1:1 mixtures of heterothallic $h^+ \times h^-$ cells (also called P × M cells) were used as indicated. Minimal sporulation liquid (MSL) media with or without nitrogen (MSL+N and MSL−N) liquid or agar were used to grow and mate the cells, respectively (Egel et al., 1994). All live-cell imaging was performed on cells placed on MSL−N with 2% electrophoresis-grade agarose pads, covered with a coverslip sealed with VALAP (1:1:1 Vaseline/lanolin/paraffin).

Genes were tagged at their endogenous genomic locus at their 3′ end, yielding C-terminally tagged proteins. This was achieved by PCR amplification of a fragment from a template plasmid with primers carrying 5′ extensions corresponding to the last 80 nucleotides of the ORF and the first 80 nucleotides of the 3′UTR, which was transformed and integrated in the genome by homologous recombination, as previously described (Bähler et al., 1998). For tagging of genes with sfGFP, a pFA6a-sfGFP-kanMX plasmid was used as a template. sfGFP was amplified from pMaM4 (a plasmid provided by M. Knop, University of Heidelberg, Heidelberg, Germany; containing yeast codon-optimized sfGFP), with primers osm2680 (5′-ccTTAATTAActccaagggtgaagagctatttac-3′; PacI site uppercase) and osm2681 (5′-aGGCGCGCCttataaagctcgtccattccg-3′; AscI site uppercase), digested with AscI and Pac1 and ligated to similarly treated pSM674 (pFA6a-EGFP-kanMX6; described in Bähler et al., 1998). The sfGFP replaced EGFP, resulting in pFA6a-sfGFP-kanMX6 (pSM1538). We then used this vector as template for PCR-based targeted tagging of fus1, agn2, eng2, and exg3 (Bähler et al., 1998).

To yield P^{map3}-driven fluorescent reporters, the *map3* promoter region was amplified from genomic DNA with primers osm935 (5′-cccCTGCAGaagcatgcacgctgctcac-3′; PstI site uppercase) and osm936 (5′-agaGTCGACggtaaactcaacgtataag-3′; SalI site uppercase), digested with Pst1 and SalI, and ligated to similarly treated pSM242 (pRIP42:GFP; an integrative plasmid containing GFP under control of *nmt41* promoter and a *ura4*$^+$ selection marker), replacing the *nmt41* promoter and yielding plasmid pSM793 (pRIP-P^{map3}:GFP, ura4$^+$). To generate a red reporter, the tdTomato tandem repeat was amplified from pFA6a-tdTomato-kanMX with primers osm944 (5′-aatGGATCCatggtgagcaagggcgaggaggtc-3′; BamHI site uppercase) and osm945 (5′-ttaCCCGGGcttgtacagctcgtccatgc-3′; XmaI site uppercase), digested with BamHI and XmaI, and ligated to similarly treated pSM793, yielding plasmid pSM1709 (pRIP-P^{map3}:tdTomato; ura4$^+$). Plasmids were linearized with NruI and integrated at the map3 promoter in h90 cells.

Mating assays

Mating assays were performed as in Bendezú and Martin (2013). In brief, precultures of cells were grown at 25°C to reach an OD600 of between 0.4 and 1 in MSL+N. Cultures were then diluted to an OD600 of 0.025 in MSL+N (for heterothallic crosses, cells were mixed in equal parts) and grown for 18–20 h to an OD600 of between 0.4 and 1 at 25°C, or 30°C for slow growing mutants (*for3Δ* and myosin deletion mutants), in MSL+N. Cells were pelleted by centrifugation and washed three times with MSL−N. Cells were then added onto MSL−N + 2% electrophoresis-grade agarose pads and incubated either at 25°C for 1 h before imaging in overnight videos or at 18°C overnight before imaging. For fusion efficiency, the total number of mating pairs and the number of fused mating pairs were quantified using the ObjectJ plugin in ImageJ (National Institutes of Health). Fused mating pairs were identified in differential interference contrast images as asci containing ascospores or mating pairs without residual cell wall between them. The obtained data were used to calculate fusion efficiency = (number of fused mating pairs/total number of mating pairs) × 100 and the mating efficiency = (number of mating pairs × 2/total number of cells) × 100 for each crossing. Fusion efficiencies of *h90* wild-type or $h^+ \times h^-$ wild-type matings were identical. We also verified that tagging of Myo52 did not affect fusion efficiency.

Microscopy and image analysis

A DeltaVision epifluorescence system and/or a spinning-disk confocal microscope were used to acquire images. Wide-field microscopy was performed on a DeltaVision platform (Applied Precision) composed of a customized inverted microscope (IX-71; Olympus), a UPlan Apochromat 100×/1.4 NA oil objective, a camera (CoolSNAP HQ2; Photometrics), and a color combined unit illuminator (Insight SSI 7; Social Science Insights). Figures were acquired using softWoRx v4.1.2 software (Applied Precision). Spinning-disk microscopy was performed using an inverted microscope (DMI4000B; Leica) equipped with an HCX Plan Apochromat 100×/1.46 NA oil objective and an UltraVIEW system (PerkinElmer; including a real-time confocal scanning head [CSU22; Yokagawa Electric Corporation], solid-state laser lines, and an electron-multiplying charge-coupled device camera [C9100; Hamamatsu Photonics]). Stacks of z-series confocal sections were acquired at 0.3-µm intervals using Volocity software (PerkinElmer).

The DeltaVision platform was used for quantitative analyses of mating and fusion efficiency and overnight videos, whereas the spinning disk

Downloaded from jcb.rupress.org on March 31, 2015

Published March 30, 2015

was used for high-temporal resolution images to study the transitions between the fusion steps as well as z-stack maximal projection images (Fig. 2, A and H; Fig. 3, D, H, and I; Fig. 4, C and G; Fig. 5, A and D–G; Fig. S1; Fig. S2, A–H; and Fig. S3 C). The DeltaVision platform was described previously (Bendezú and Martin, 2013). To limit photobleaching, overnight videos were captured by optical axis integration imaging of a 4.6-µm z section, which is essentially a real-time z sweep (Fig. 1, A–C; Fig. 2, B–E; Fig. 3 A; Fig. 4, B and E; and Fig. S3 B). The spinning-disk microscope system was as previously described (Bendezú et al., 2012). For spinning-disk confocal imaging, optical slices were acquired every 0.6 µm, and all panels show maximum projections, unless otherwise indicated. Time projections are sum projections of time-lapse series, made using ImageJ. All imaging, except for *cdc12-112*^{ts} mutants and control strains (Fig. S2, D and E), was performed at room temperature (~22°C). *cdc12-112*^{ts} mutant strains were imaged at 33°C using an objective heater.

Actin phalloidin staining was performed using Alexa Fluor 488–phalloidin (Invitrogen). Mating reactions were performed on MSL−N agar plates for 18–20 h at 25°C. Mating cells were then scratched off the plates and added directly into PM buffer (35 mM K-phosphate buffer 6, pH 6.8, and 0.5 mM $MgSO_4$) with 4% formaldehyde for 30 min. The cells were then washed three times with PM buffer and span down at 1,000 rpm for 3 min, permeabilized in PM buffer with 0.5% Triton X-100 for 30 s, and washed again three times before adding 10 µl of Alexa Fluor 488–phalloidin to 5 µl of concentrated sample. Calcofluor (Sigma-Aldrich) was added at a final concentration of 5 µg/ml from a 200× stock solution (1 mg/ml; Fig. 5 C).

FRAP was performed with the photokinesis unit of the spinning-disk system (Bendezú and Martin, 2011). A circular 0.9-µm zone was photobleached using maximal laser power at the shmoo tip or the cell tip for cells during mitotic growth. In cells with a fusion focus, the 0.9-µm circular zone was centered over the fusion focus and photobleached the entire structure. Initial FRAP experiments (Figs. 3 C and S3 A) were conducted in *h90* homothallic crosses, photobleaching, and recording recovery of the fluorescent Myo52 signal in both partner cells. To probe the specific dynamics in each mating type (Fig. 3 G), heterothallic crosses with GFP-CHD–tagged cells were used. Images were recorded before photobleaching and immediately after, every second for 90 s. Kymographs at the fusion site (Fig. 3, D and H) were constructed in ImageJ v1.46 by drawing a 3-pixel-wide (0.39 µm) line connecting the myosins dots in both partner cells. FRAP measurements were performed as previously published (Bendezú et al., 2012). In brief, for FRAP analysis, the mean fluorescence intensities were measures over time in three regions: (1) the photobleached region, (2) the background outside the cell, and (3) another nonbleached cell. The background fluorescence was subtracted from the fluorescence intensities of the photobleached and the nonbleached cell. The loss of signal as a result of imaging was corrected by dividing the adjusted bleached regions intensity by the adjusted intensity of the nonbleached cell. All values were normalized so that the prephotobleaching value equals 1.

GFP-CHD intensity at the fusion focus (Fig. 1 D) was measured in ImageJ within a manually drawn box of ~40 × 40 pixels at the cell–cell contact zone over time. Background fluorescence outside the cell was measured within a box of same dimensions and was then subtracted from the GFP-CHD fluorescence measurements at the fusion site. Fluorescence was then normalized to the maximum intensity signal. Fusion time was defined by the sudden increase in the intensity of tdTomato in the h^- partner cell, which was measured within a box of 50 × 50 pixels positioned in the center of the h^+ partner cell. Background signal was subtracted similarly as for GFP-CHD and then normalized to the maximum intensity signal. Fluorescence signals were then aligned to fusion time and averaged. The distance between Myo52 signals was measured on time-lapse videos of *h*$^-$ *myo52-GFP* crossed to *h*$^+$ *myo52-tdTomato* (Fig. 3 B), using the ImageJ line measure tool to measure the distance between the highest intensity pixel of the Myo52-tdTomato and Myo52-GFP signals.

The displacement of Myo52 signal (Fig. 3, E and F) was measured by following the x and y coordinates of the highest intensity pixel of the Myo52-tdTomato signal in each mating partner over time. The homothallic strain used, also expressed *p*^{map3}*:GFP* as a marker for the mating type. Time interval of the video is 7.2 min. During the Myo52 crescent phase, we recorded the coordinates of the maximum fluorescence intensity. Displacement was then calculated as

$$\sqrt{(X_n - X_{n-1})^2 + (Y_n - Y_{n-1})^2}.$$

For Fig. 3 F, the mean instantaneous displacement over the course of fusion was calculated for each cell. The graph shows n mean over eight cells.

Fluorescence intensities of Myo52-tdTomato and Myo51-3YFP signals in Fig. S3 B were measured in ImageJ using a manually drawn box of 40 × 30 pixels surrounding the contact zone of each mating partner. Background fluorescence for YFP and tomato were measured over time and subtracted from the original measurements. The fluorescence signal was normalized to the maximum intensity signal.

Structured illumination images (Fig. 2 F and Videos 3 and 4) were acquired using a Nikon SIM setup (Eclipse T1 microscope fitted with a super-resolution Apochromat total internal reflection fluorescence 100×/1.49 NA objective and an electron-multiplying charge-coupled device camera (IXON3; Andor Technology). Imaging was performed at 3.4-s interval in 3D SIM acquisition mode (15 image per plane; five phases of three rotations) with an 80-ms exposure time using a 488-nm coherent sapphire laser at 1.30 mW (measured in the back focal plane of the objective). Image reconstruction was performed using the NIS-Elements software (Nikon; based on Gustafsson et al., 2008); reconstruction parameters were as follows: contrast 0.70; apodization 1.00; and Widh3DFilter 0.20.

Laser-scanning confocal microscopy (Videos 5 and 6) was performed on a microscope (LSM 710; Carl Zeiss) with external-port GaAsP detectors. Pinhole was reduced to 0.5 arbitrary units, and the 488-nm argon laser line was set to 0.15 mW (in the backfocal plane of the objective) to easily observe actin filaments.

Figures were assembled with Photoshop CS5 (Adobe) and Illustrator CS5 (Adobe). All error bars are standard deviations of the number of indicated samples (cells or actin cables) analyzed, except for Fig. 1 B, Fig. 4 (A, F, and H), Fig. 5 B, and Fig. S2 E, in which the error bars are standard deviations of three independent experiments. All experiments were performed a minimum of three independent times except for Fig. 2 (F and G), Fig. 3 C, Fig. S2 C, and Fig. S3 A, which were performed two independent times.

Online supplemental material

Fig. S1 (related to Fig. 1) shows Fus1-dependent actin accumulation at the prospective fusion site. Fig. S2 (related to Fig. 2) shows fusion focus formation is independent of formins For3 and Cdc12 and of actin patch components. Fig. S3 (related to Fig. 4) shows type V myosin localization and dynamics define multiple steps in the formation of the fusion focus. Table S1 shows strains used in this study. Video 1 (related to Fig. 1) shows an actin fusion focus forms before cell fusion. Video 2 (related to Fig. 1) shows absence of actin fusion focus in *fus1Δ*. Video 3 (related to Fig. 2) shows the actin fusion focus visualized by 3D SIM. Video 4 (related to Fig. 2) shows the actin fusion focus visualized by 3D SIM in *for3Δ*. Video 5 (related to Fig. 2) shows actin at the zone of cell–cell contact visualized by 3D SIM in *fus1Δ*. Video 6 (related to Fig. 2) shows actin at the zone of cell–cell contact visualized by 3D SIM in *fus1Δ for3Δ*. Video 7 (related to Fig. 2) shows the actin fusion focus visualized by scanning confocal microscopy in wild type and *for3Δ*. Video 8 (related to Fig. 2) shows actin at the zone of cell–cell contact visualized by scanning confocal microscopy in *fus1Δ* and *fus1Δ for3Δ*. Video 9 (related to Fig. 3) shows asymmetric maturation of the fusion focus. Online supplemental material is available at http://www.jcb.org/cgi/content/full/jcb.201411124/DC1. Additional data are available in the JCB DataViewer at http://dx.doi.org/10.1083/jcb.201411124.dv.

We thank Fred Chang, Kathy Gould, Michael Knop, David Kovar, Olaf Nielsen, Thomas Pollard, Yolanda Sanchez, Chikashi Shimoda, Vladimir Sirotkin, and Carlos R. Vàzquez de Aldana for strains and reagents; the Martin laboratory for discussion; and Richard Benton, Serge Pelet, and members of the Martin and Pelet laboratories for comments on the manuscript.

This work was supported by a European Research Council Starting grant (260493) and a Swiss National Science Foundation (SNF) research grant (31003A_138177) to S.G. Martin. The SIM microscope was funded via an SNF R'equip grant.

The authors declare no competing financial interests.

Submitted: 28 November 2014
Accepted: 25 February 2015

References

Abmayr, S.M., and G.K. Pavlath. 2012. Myoblast fusion: lessons from flies and mice. *Development.* 139:641–656. http://dx.doi.org/10.1242/dev.068353

Aguilar, P.S., M.K. Baylies, A. Fleissner, L. Helming, N. Inoue, B. Podbilewicz, H. Wang, and M. Wong. 2013. Genetic basis of cell-cell fusion mechanisms. *Trends Genet.* 29:427–437. http://dx.doi.org/10.1016/j.tig.2013.01.011

Downloaded from jcb.rupress.org on March 31, 2015

Published March 30, 2015

Ayscough, K.R., and D.G. Drubin. 1998. A role for the yeast actin cytoskeleton in pheromone receptor clustering and signalling. *Curr. Biol.* 8:927–930. http://dx.doi.org/10.1016/S0960-9822(07)00374-0

Bagnat, M., and K. Simons. 2002. Cell surface polarization during yeast mating. *Proc. Natl. Acad. Sci. USA*. 99:14183–14188. http://dx.doi.org/10.1073/pnas.172517799

Bähler, J., J.Q. Wu, M.S. Longtine, N.G. Shah, A. McKenzie III, A.B. Steever, A. Wach, P. Philippsen, and J.R. Pringle. 1998. Heterologous modules for efficient and versatile PCR-based gene targeting in *Schizosaccharomyces pombe*. *Yeast*. 14:943–951. http://dx.doi.org/10.1002/(SICI)1097-0061(199807)14:10<943::AID-YEA292>3.0.CO;2-Y

Bendezú, F.O., and S.G. Martin. 2011. Actin cables and the exocyst form two independent morphogenesis pathways in the fission yeast. *Mol. Biol. Cell*. 22:44–53. http://dx.doi.org/10.1091/mbc.E10-08-0720

Bendezú, F.O., and S.G. Martin. 2013. Cdc42 explores the cell periphery for mate selection in fission yeast. *Curr. Biol.* 23:42–47. http://dx.doi.org/10.1016/j.cub.2012.10.042

Bendezú, F.O., V. Vincenzetti, and S.G. Martin. 2012. Fission yeast Sec3 and Exo70 are transported on actin cables and localize the exocyst complex to cell poles. *PLoS ONE*. 7:e40248. http://dx.doi.org/10.1371/journal.pone.0040248

Brizzio, V., A.E. Gammie, G. Nijbroek, S. Michaelis, and M.D. Rose. 1996. Cell fusion during yeast mating requires high levels of a-factor mating pheromone. *J. Cell Biol.* 135:1727–1739. http://dx.doi.org/10.1083/jcb.135.6.1727

Brizzio, V., A.E. Gammie, and M.D. Rose. 1998. Rvs161p interacts with Fus2p to promote cell fusion in *Saccharomyces cerevisiae*. *J. Cell Biol.* 141:567–584. http://dx.doi.org/10.1083/jcb.141.3.567

Cappellaro, C., V. Mrsa, and W. Tanner. 1998. New potential cell wall glucanases of *Saccharomyces cerevisiae* and their involvement in mating. *J. Bacteriol.* 180:5030–5037.

Cortés, J.C., J. Ishiguro, A. Durán, and J.C. Ribas. 2002. Localization of the (1,3)beta-D-glucan synthase catalytic subunit homologue Bgs1p/Cps1p from fission yeast suggests that it is involved in septation, polarized growth, mating, spore wall formation and spore germination. *J. Cell Sci.* 115:4081–4096. http://dx.doi.org/10.1242/jcs.00085

Cortés, J.C., E. Carnero, J. Ishiguro, Y. Sánchez, A. Durán, and J.C. Ribas. 2005. The novel fission yeast (1,3)beta-D-glucan synthase catalytic subunit Bgs4p is essential during both cytokinesis and polarized growth. *J. Cell Sci.* 118:157–174. http://dx.doi.org/10.1242/jcs.01585

Dekker, N., D. Speijer, C.H. Grün, M. van den Berg, A. de Haan, and F. Hochstenbach. 2004. Role of the alpha-glucanase Agn1p in fission-yeast cell separation. *Mol. Biol. Cell*. 15:3903–3914. http://dx.doi.org/10.1091/mbc.E04-04-0319

Dekker, N., J. van Rijssel, B. Distel, and F. Hochstenbach. 2007. Role of the alpha-glucanase Agn2p in ascus-wall endolysis following sporulation in fission yeast. *Yeast*. 24:279–288. http://dx.doi.org/10.1002/yea.1464

Dorer, R., C. Boone, T. Kimbrough, J. Kim, and L.H. Hartwell. 1997. Genetic analysis of default mating behavior in *Saccharomyces cerevisiae*. *Genetics*. 146:39–55.

Doyle, A., R. Martín-García, A.T. Coulton, S. Bagley, and D.P. Mulvihill. 2009. Fission yeast Myo51 is a meiotic spindle pole body component with discrete roles during cell fusion and spore formation. *J. Cell Sci.* 122:4330–4340. http://dx.doi.org/10.1242/jcs.055202

Dueñas-Santero, E., A.B. Martín-Cuadrado, T. Fontaine, J.P. Latgé, F. del Rey, and C. Vázquez de Aldana. 2010. Characterization of glycoside hydrolase family 5 proteins in *Schizosaccharomyces pombe*. *Eukaryot. Cell*. 9:1650–1660. http://dx.doi.org/10.1128/EC.00187-10

Egel, R., M. Willer, S. Kjaerulff, J. Davey, and O. Nielsen. 1994. Assessment of pheromone production and response in fission yeast by a halo test of induced sporulation. *Yeast*. 10:1347–1354. http://dx.doi.org/10.1002/yea.320101012

Encinar del Dedo, J., E. Dueñas, Y. Arnáiz, F. del Rey, and C.R. Vázquez de Aldana. 2009. β-glucanase Eng2 is required for ascus wall endolysis after sporulation in the fission yeast *Schizosaccharomyces pombe*. *Eukaryot. Cell*. 8:1278–1286. http://dx.doi.org/10.1128/EC.00148-09

Feierbach, B., and F. Chang. 2001. Roles of the fission yeast formin for3p in cell polarity, actin cable formation and symmetric cell division. *Curr. Biol.* 11:1656–1665. http://dx.doi.org/10.1016/S0960-9822(01)00525-5

Gammie, A.E., V. Brizzio, and M.D. Rose. 1998. Distinct morphological phenotypes of cell fusion mutants. *Mol. Biol. Cell*. 9:1395–1410. http://dx.doi.org/10.1091/mbc.9.6.1395

Goshima, G., F. Nédélec, and R.D. Vale. 2005. Mechanisms for focusing mitotic spindle poles by minus end–directed motor proteins. *J. Cell Biol.* 171:229–240. http://dx.doi.org/10.1083/jcb.200505107

Gustafsson, M.G., L. Shao, P.M. Carlton, C.J. Wang, I.N. Golubovskaya, W.Z. Cande, D.A. Agard, and J.W. Sedat. 2008. Three-dimensional resolution doubling in wide-field fluorescence microscopy by structured illumination. *Biophys. J.* 94:4957–4970. http://dx.doi.org/10.1529/biophysj.107.120345

Heald, R., R. Tournebize, A. Habermann, E. Karsenti, and A. Hyman. 1997. Spindle assembly in *Xenopus* egg extracts: respective roles of centrosomes and microtubule self-organization. *J. Cell Biol.* 138:615–628. http://dx.doi.org/10.1083/jcb.138.3.615

Huberman, L.B., and A.W. Murray. 2014. A model for cell wall dissolution in mating yeast cells: polarized secretion and restricted diffusion of cell wall remodeling enzymes induces local dissolution. *PLoS ONE*. 9:e109780. http://dx.doi.org/10.1371/journal.pone.0109780

Itadani, A., T. Nakamura, and C. Shimoda. 2006. Localization of type I myosin and F-actin to the leading edge region of the forespore membrane in *Schizosaccharomyces pombe*. *Cell Struct. Funct.* 31:181–195. http://dx.doi.org/10.1247/csf.06027

Iwaki, T., N. Tanaka, H. Takagi, Y. Giga-Hama, and K. Takegawa. 2004. Characterization of end4+, a gene required for endocytosis in *Schizosaccharomyces pombe*. *Yeast*. 21:867–881. http://dx.doi.org/10.1002/yea.1134

Kamasaki, T., R. Arai, M. Osumi, and I. Mabuchi. 2005. Directionality of F-actin cables changes during the fission yeast cell cycle. *Nat. Cell Biol.* 7:916–917. http://dx.doi.org/10.1038/ncb1295

Kamasaki, T., M. Osumi, and I. Mabuchi. 2007. Three-dimensional arrangement of F-actin in the contractile ring of fission yeast. *J. Cell Biol.* 178:765–771. http://dx.doi.org/10.1083/jcb.200612018

Karagiannis, J., A. Bimbó, S. Rajagopalan, J. Liu, and M.K. Balasubramanian. 2005. The nuclear kinase Lsk1p positively regulates the septation initiation network and promotes the successful completion of cytokinesis in response to perturbation of the actomyosin ring in *Schizosaccharomyces pombe*. *Mol. Biol. Cell*. 16:358–371. http://dx.doi.org/10.1091/mbc.E04-06-0502

Kim, S., K. Shilagardi, S. Zhang, S.N. Hong, K.L. Sens, J. Bo, G.A. Gonzalez, and E.H. Chen. 2007. A critical function for the actin cytoskeleton in targeted exocytosis of prefusion vesicles during myoblast fusion. *Dev. Cell*. 12:571–586. http://dx.doi.org/10.1016/j.devcel.2007.02.019

Kovar, D.R., V. Sirotkin, and M. Lord. 2011. Three's company: the fission yeast actin cytoskeleton. *Trends Cell Biol.* 21:177–187. http://dx.doi.org/10.1016/j.tcb.2010.11.001

Kurahashi, H., Y. Imai, and M. Yamamoto. 2002. Tropomyosin is required for the cell fusion process during conjugation in fission yeast. *Genes Cells*. 7:375–384. http://dx.doi.org/10.1046/j.1365-2443.2002.00526.x

Linder, S. 2007. The matrix corroded: podosomes and invadopodia in extracellular matrix degradation. *Trends Cell Biol.* 17:107–117. http://dx.doi.org/10.1016/j.tcb.2007.01.002

Liu, H., and A. Bretscher. 1992. Characterization of TPM1 disrupted yeast cells indicates an involvement of tropomyosin in directed vesicular transport. *J. Cell Biol.* 118:285–299. http://dx.doi.org/10.1083/jcb.118.2.285

Lo Presti, L., and S.G. Martin. 2011. Shaping fission yeast cells by rerouting actin-based transport on microtubules. *Curr. Biol.* 21:2064–2069. http://dx.doi.org/10.1016/j.cub.2011.10.033

Lo Presti, L., F. Chang, and S.G. Martin. 2012. Myosin Vs organize actin cables in fission yeast. *Mol. Biol. Cell*. 23:4579–4591. http://dx.doi.org/10.1091/mbc.E12-07-0499

Maiato, H., C.L. Rieder, and A. Khodjakov. 2004. Kinetochore-driven formation of kinetochore fibers contributes to spindle assembly during animal mitosis. *J. Cell Biol.* 167:831–840. http://dx.doi.org/10.1083/jcb.200407090

Martin, S.G., and F. Chang. 2006. Dynamics of the formin for3p in actin cable assembly. *Curr. Biol.* 16:1161–1170. http://dx.doi.org/10.1016/j.cub.2006.04.040

Martín-Cuadrado, A.B., E. Dueñas, M. Sipiczki, C.R. Vázquez de Aldana, and F. del Rey. 2003. The endo-beta-1,3-glucanase eng1p is required for dissolution of the primary septum during cell separation in *Schizosaccharomyces pombe*. *J. Cell Sci.* 116:1689–1698. http://dx.doi.org/10.1242/jcs.00377

Martín-Cuadrado, A.B., T. Fontaine, P.F. Esteban, J.E. del Dedo, M. de Medina-Redondo, F. del Rey, J.P. Latgé, and C.R. de Aldana. 2008. Characterization of the endo-beta-1,3-glucanase activity of *S. cerevisiae* Eng2 and other members of the GH81 family. *Fungal Genet. Biol.* 45:542–553. http://dx.doi.org/10.1016/j.fgb.2007.09.001

Massarwa, R., S. Carmon, B.Z. Shilo, and E.D. Schejter. 2007. WIP/WASp-based actin-polymerization machinery is essential for myoblast fusion in *Drosophila*. *Dev. Cell*. 12:557–569. http://dx.doi.org/10.1016/j.devcel.2007.01.016

Mata, J., and J. Bähler. 2006. Global roles of Ste11p, cell type, and pheromone in the control of gene expression during early sexual differentiation in fission yeast. *Proc. Natl. Acad. Sci. USA*. 103:15517–15522. http://dx.doi.org/10.1073/pnas.0603403103

Merlini, L., O. Dudin, and S.G. Martin. 2013. Mate and fuse: how yeast cells do it. *Open Biol*. 3:130008. http://dx.doi.org/10.1098/rsob.130008

Motegi, F., R. Arai, and I. Mabuchi. 2001. Identification of two type V myosins in fission yeast, one of which functions in polarized cell growth and moves rapidly in the cell. *Mol. Biol. Cell*. 12:1367–1380. http://dx.doi.org/10.1091/mbc.12.5.1367

Downloaded from jcb.rupress.org on March 31, 2015

Published March 30, 2015

Mulvihill, D.P., S.R. Edwards, and J.S. Hyams. 2006. A critical role for the type V myosin, Myo52, in septum deposition and cell fission during cytokinesis in *Schizosaccharomyces pombe*. *Cell Motil. Cytoskeleton*. 63:149–161. http://dx.doi.org/10.1002/cm.20113

Paterson, J.M., C.A. Ydenberg, and M.D. Rose. 2008. Dynamic localization of yeast Fus2p to an expanding ring at the cell fusion junction during mating. *J. Cell Biol.* 181:697–709.

Pédelacq, J.D., S. Cabantous, T. Tran, T.C. Terwilliger, and G.S. Waldo. 2006. Engineering and characterization of a superfolder green fluorescent protein. *Nat. Biotechnol.* 24:79–88. http://dx.doi.org/10.1038/nbt1172

Pérez, P., and J.C. Ribas. 2004. Cell wall analysis. *Methods*. 33:245–251. http://dx.doi.org/10.1016/j.ymeth.2003.11.020

Petersen, J., D. Weilguny, R. Egel, and O. Nielsen. 1995. Characterization of fus1 of *Schizosaccharomyces pombe*: a developmentally controlled function needed for conjugation. *Mol. Cell. Biol.* 15:3697–3707.

Petersen, J., O. Nielsen, R. Egel, and I.M. Hagan. 1998a. F-actin distribution and function during sexual differentiation in *Schizosaccharomyces pombe*. *J. Cell Sci.* 111:867–876.

Petersen, J., O. Nielsen, R. Egel, and I.M. Hagan. 1998b. FH3, a domain found in formins, targets the fission yeast formin Fus1 to the projection tip during conjugation. *J. Cell Biol.* 141:1217–1228. http://dx.doi.org/10.1083/jcb.141.5.1217

Richardson, B.E., K. Beckett, S.J. Nowak, and M.K. Baylies. 2007. SCAR/WAVE and Arp2/3 are crucial for cytoskeletal remodeling at the site of myoblast fusion. *Development*. 134:4357–4367. http://dx.doi.org/10.1242/dev.010678

Rojas, E.R., S. Hotton, and J. Dumais. 2011. Chemically mediated mechanical expansion of the pollen tube cell wall. *Biophys. J.* 101:1844–1853. http://dx.doi.org/10.1016/j.bpj.2011.08.016

Scott, B.J., E.M. Neidt, and D.R. Kovar. 2011. The functionally distinct fission yeast formins have specific actin-assembly properties. *Mol. Biol. Cell*. 22:3826–3839. http://dx.doi.org/10.1091/mbc.E11-06-0492

Sens, K.L., S. Zhang, P. Jin, R. Duan, G. Zhang, F. Luo, L. Parachini, and E.H. Chen. 2010. An invasive podosome-like structure promotes fusion pore formation during myoblast fusion. *J. Cell Biol.* 191:1013–1027. http://dx.doi.org/10.1083/jcb.201006006

Sheltzer, J.M., and M.D. Rose. 2009. The class V myosin Myo2p is required for Fus2p transport and actin polarization during the yeast mating response. *Mol. Biol. Cell*. 20:2909–2919. http://dx.doi.org/10.1091/mbc.E08-09-0923

Shilagardi, K., S. Li, F. Luo, F. Marikar, R. Duan, P. Jin, J.H. Kim, K. Murnen, and E.H. Chen. 2013. Actin-propelled invasive membrane protrusions promote fusogenic protein engagement during cell-cell fusion. *Science*. 340:359–363. http://dx.doi.org/10.1126/science.1234781

Skoumpla, K., A.T. Coulton, W. Lehman, M.A. Geeves, and D.P. Mulvihill. 2007. Acetylation regulates tropomyosin function in the fission yeast *Schizosaccharomyces pombe*. *J. Cell Sci.* 120:1635–1645. http://dx.doi.org/10.1242/jcs.001115

Surrey, T., F. Nedelec, S. Leibler, and E. Karsenti. 2001. Physical properties determining self-organization of motors and microtubules. *Science*. 292:1167–1171. http://dx.doi.org/10.1126/science.1059758

Tanaka, H., E. Takasu, T. Aigaki, K. Kato, S. Hayashi, and A. Nose. 2004. Formin3 is required for assembly of the F-actin structure that mediates tracheal fusion in *Drosophila*. *Dev. Biol.* 274:413–425. http://dx.doi.org/10.1016/j.ydbio.2004.07.035

Tokuo, H., K. Mabuchi, and M. Ikebe. 2007. The motor activity of myosin-X promotes actin fiber convergence at the cell periphery to initiate filopodia formation. *J. Cell Biol.* 179:229–238. http://dx.doi.org/10.1083/jcb.200703178

Wang, N., L. Lo Presti, Y.H. Zhu, M. Kang, Z. Wu, S.G. Martin, and J.Q. Wu. 2014. The novel proteins Rng8 and Rng9 regulate the myosin-V Myo51 during fission yeast cytokinesis. *J. Cell Biol.* 205:357–375. http://dx.doi.org/10.1083/jcb.201308146

Win, T.Z., Y. Gachet, D.P. Mulvihill, K.M. May, and J.S. Hyams. 2001. Two type V myosins with non-overlapping functions in the fission yeast *Schizosaccharomyces pombe*: Myo52 is concerned with growth polarity and cytokinesis, Myo51 is a component of the cytokinetic actin ring. *J. Cell Sci.* 114:69–79.

Xue-Franzén, Y., S. Kjaerulff, C. Holmberg, A. Wright, and O. Nielsen. 2006. Genomewide identification of pheromone-targeted transcription in fission yeast. *BMC Genomics*. 7:303. http://dx.doi.org/10.1186/1471-2164-7-303

Ydenberg, C.A., R.A. Stein, and M.D. Rose. 2012. Cdc42p and Fus2p act together late in yeast cell fusion. *Mol. Biol. Cell*. 23:1208–1218. http://dx.doi.org/10.1091/mbc.E11-08-0723

Zhou, Z., E.L. Munteanu, J. He, T. Ursell, M. Bathe, K.C. Huang, and F. Chang. 2015. The contractile ring coordinates curvature-dependent septum assembly during fission yeast cytokinesis. *Mol. Biol. Cell*. 26:78–90. http://dx.doi.org/10.1091/mbc.E14-10-1441

Downloaded from jcb.rupress.org on March 31, 2015

Dudin et al., http://www.jcb.org/cgi/content/full/jcb.201411124/DC1

THE JOURNAL OF CELL BIOLOGY

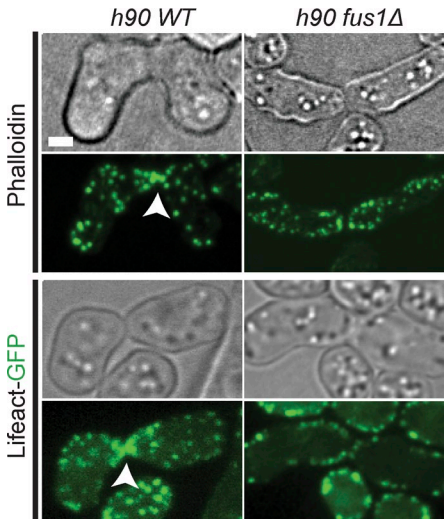

Figure S1. **Fus1-dependent actin accumulation at the prospective fusion site.** (Related to Fig. 1.) Images of homothallic wild-type (WT) *h90* strains (left) fixed and stained with Alex Fluor–phalloidin (top) or live expressing LifeAct-GFP. The arrowheads indicate actin accumulation at the fusion site. (right) In contrast, no actin accumulation is observed in *h90 fus1Δ* strains. Bar, 1 µm.

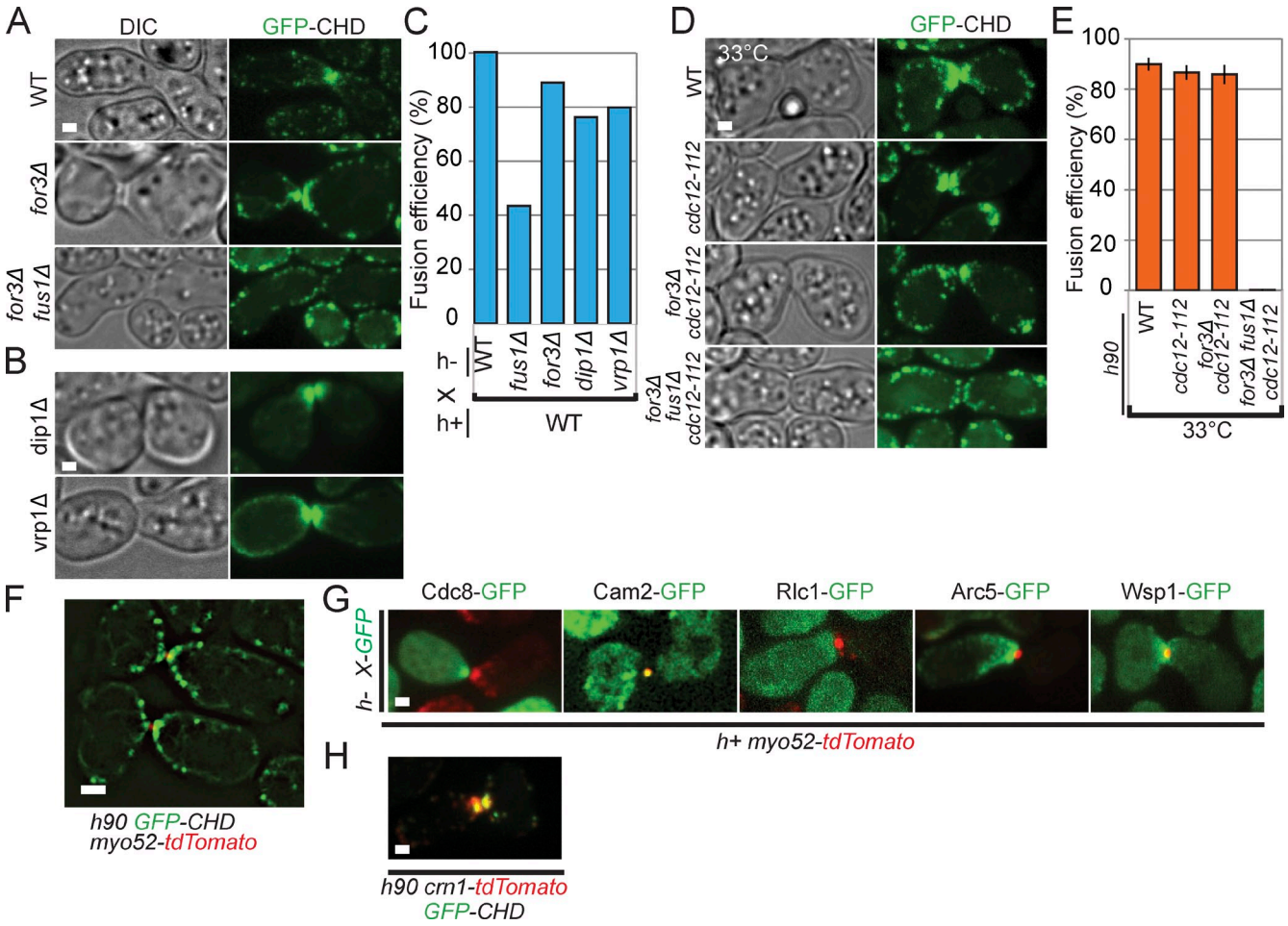

Figure S2. **Fusion focus formation is independent of formins For3 and Cdc12 and of actin patch components.** (Related to Fig. 2.) (A) Homothallic *h90 wild-type* (WT), *for3Δ*, and *for3Δ fus1Δ* strains expressing GFP-CHD. An actin focus forms in *for3Δ* but not in *for3Δ fus1Δ*. (B) Homothallic *h90 dip1Δ* and *vrp1Δ* strains expressing GFP-CHD, in which the fusion focus forms normally. (C) Fusion efficiency of indicated heterothallic crosses, $n > 90$. (D) Homothallic *h90 wild-type*, *cdc12-112*, *cdc12-112 for3Δ*, and *cdc12-112 for3Δ fus1Δ* strains expressing GFP-CHD imaged at 33°C. An actin focus forms in all cases, except upon *fus1* deletion. Note the presence of some aberrant actin structures in the *cdc12-112 for3Δ* double mutant. (E) Fusion efficiency of homothallic *h90 wild-type*, *cdc12-112*, *cdc12-112 for3Δ*, and *cdc12-112 for3Δ fus1Δ* mutants at 33°C. For3 and Cdc12 do not contribute during cell–cell fusion. Error bars are standard deviations. (F) 3D SIM of GFP-CHD and Myo52-tdTomato colocalization in homothallic *h90 wild type*. This image represents the same cell pair as shown in Fig. 2 F, after which time-lapse imaging of only the GFP channel was acquired. (G) Heterothallic h^- strains expressing indicated GFP fusions crossed to h^+ *myo52-tdTomato* cells. Cdc8 tropomyosin and Cam2 calmodulin form a dot at the fusion site, but not Rlc1, Arc5, or Wsp1. (H) Homothallic *h90 crn1-tdTomato GFP-CHD*. Crn1 coronin decorates the fusion focus. DIC, differential interference contrast. Bars, 1 µm.

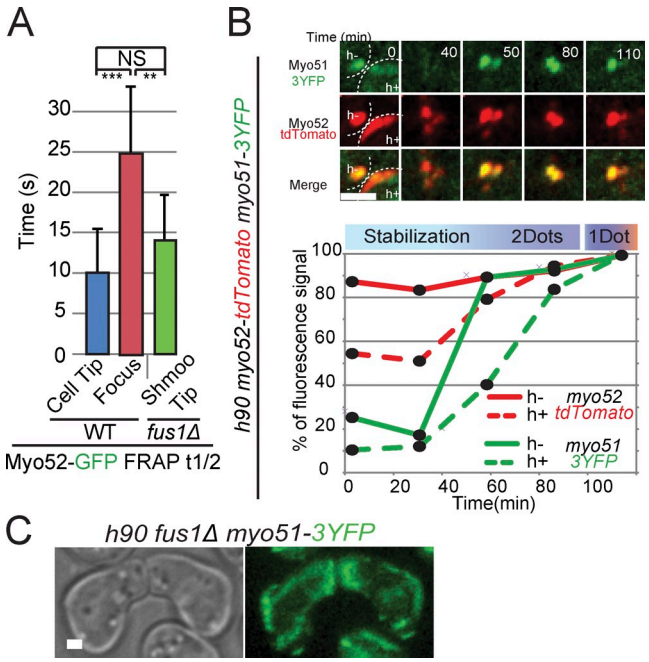

Figure S3. **Type V myosin localization and dynamics define multiple steps in the formation of the fusion focus.** (Related to Fig. 4.) (A) Mean FRAP recovery half-times of Myo52-GFP at the cell tip of vegetative growing cells or during cell–cell fusion in presence or absence of Fus1. Myo52 lower mobility at the fusion focus depends on Fus1. Note that the half-time values measured with Myo52-GFP are somewhat larger than those measured using Myo52-tdTomato (see Fig. 3 C), but the differences between focus and cell tip are similar. *t* test, ***, $P = 6.9 \times 10^{-10}$; **, $P = 1.3 \times 10^{-4}$; $n > 12$ for each category. Error bars are standard deviations. WT, wild type. (B, top) Detail of the contact zone of a homothallic *h90 myo52-tdTomato myo51-3YFP* mating pair. (bottom) The graph shows Myo52 and Myo51 fluorescence intensities normalized to the maximum of each fluorophore. Myo51 and Myo52 focalize first in the h^- cell. This is one representative example out of five such measured mating pairs. Cell contours are shown with dotted lines. (C) Homothallic *h90 fus1Δ myo51-3YFP* strain. Myo51 accumulates as a crescent at the shmoo tip in absence of Fus1. Bars, 1 µm.

Table S1. **Strains used in this study**

Strain number	Genotype	Source
Fig. 1		
2514	*h90 p^{map3}-tdTomato-ura4+ nmt41::GFP-CHD-leu$^+$ ade6$^-$ leu1-32 ura4-D18*	This study
2515	*h90 myo52-tdTomato-natMX nmt41::GFP-CHD-leu$^+$ ade6$^-$ leu1-32 ura4-D18*	This study
2516	*h90 fus1::LEU2 p^{map3}-tdTomato-ura4$^+$ nmt41::GFP-CHD-leu$^+$ ade6$^-$ leu1-32 ura4-D18*	This study
Fig. 2		
2515	*h90 myo52-tdTomato-natMX nmt41::GFP-CHD-leu$^+$ ade6$^-$ leu1-32 ura4-D18*	This study
2517	*h90 fus1-sfGFP-kanMX p^{map3}-tdTomato-ura4$^+$ ade6$^+$ leu1$^+$ ura4-D18*	This study
2518	*h$^+$ fus1-sfGFP-kanMX myo52-tdTomato-natMX*	This study
2519	*h$^-$ fus1-sfGFP-kanMX myo52-tdTomato-natMX*	This study
2520	*h90 myo52-GFP-kanMX leu1-32*	This study
2521	*h90 fus1::LEU2 myo52-GFP-kanMX leu1-32*	This study
740	*h$^+$ myo52-tdTomato-natMX ade6-M216 leu1-32 ura4-D18*	Laboratory stock
2522	*h90 for3::kanMX nmt41::GFP-CHD-leu$^+$ ade6$^-$ leu1-32 ura4-D18*	This study
2516	*h90 fus1::LEU2 p^{map3}-tdTomato-ura4$^+$ nmt41::GFP-CHD-leu$^+$ ade6$^-$ leu1-32 ura4-D18*	This study
2587	*h90 for3::kanMX fus1::LEU2 nmt41::GFP-CHD-leu$^+$ ade6$^-$ leu1-32 ura4-D18*	This study
2523	*h$^-$ cdc12-3GFP-kanMX myo52-tomato-natMX ade6$^-$ leu1-32 ura4-D18*	This study
2524	*h$^+$ cdc12-3GFP-kanMX myo52-tomato-natMX ade6$^-$ leu1-32 ura4-D18*	This study
2525	*h$^-$ P^{cdc15}-mEGFP-cdc15:: kanMX myo52-tdTomato-natMX ade6$^-$ leu1-32 ura4-D18*	This study
2526	*h$^+$ P^{cdc1}5-mEGFP-cdc15:: kanMX myo52-tdTomato-natMX ade6$^-$ leu1-32 ura4-D18*	This study
2527	*h$^-$ for3-3GFP-kanMX myo52-tdTomato-natMX ade6$^-$ leu1-32 ura4-D18*	This study
2528	*h$^+$ for3-3GFP-kanMX myo52-tdTomato-natMX ade6$^-$ leu1-32 ura4-D18*	This study
2529	*h90 myo52-tdTomato-natMX myo51-3YFP-kanMX leu1-32 ura4-D18*	This study
2530	*h$^-$ kanMX-P^{myo1}-mGFP-myo1 myo52-tdTomato-natMX ade6$^-$ leu1-32 ura4-D18*	This study
2531	*h$^+$ kanMX-P^{myo1}-mGFP-myo1 myo52-tdTomato-natMX ade6$^-$ leu1-32 ura4-D18*	This study
2532	*h$^-$ myo52-tdTomato-natMX dip1-GFP-kanMX ade6-M216 leu1-32 ura4-D18*	This study
2533	*h$^+$ myo52-tdTomato-natMX dip1-GFP-kanMX ade6-M216 leu1-32 ura4-D18*	This study
Fig. 3		
2515	*h90 myo52-tdTomato-NatMX nmt41::GFP-CHD-leu$^+$ ade6$^-$ leu1-32 ura4-D18*	This study
2534	*h$^-$ myo52-GFP-kanMX leu1-32*	This study
2535	*h90 myo52-tdTomato-natMX p^{map3}-GFP-ura4$^+$ ade6-M216 leu1-32 ura4-D18*	This study
952	*h$^-$ myo52-tdTomato-natMX ade6-M216 leu1-32 ura4-D18*	Laboratory stock
740	*h$^+$ myo52-tdTomato-natMX ade6-M216 leu1-32 ura4-D18*	Laboratory stock
1273	*h$^-$ nmt41::GFP-CHD-leu$^+$ ade6-M216 leu1-32 ura4-D18*	Laboratory stock
2594	*h$^+$ nmt41::GFP-CHD-leu$^+$ ade6-M216 leu1-32 ura4-D18*	This study
2529	*h90 myo52-tdTomato-natMX myo51-3YFP-kanMX leu1-32 ura4-D18*	This study
2518	*h$^+$ fus1-sfGFP-kanMX myo52-tdTomato-natMX*	This study
2519	*h$^-$ fus1-sfGFP-kanMX myo52-tdTomato-natMX*	This study
Fig. 4		
1372	*h$^-$ WT (972)*	Laboratory stock
1371	*h$^+$ WT (975)*	Laboratory stock
2536	*h$^-$ myo52::ura4$^+$ leu1$^-$ ura4-*	This study
1923	*h$^+$ myo52::ura4$^+$ leu1$^-$ ura4-*	Laboratory stock
1532	*h$^-$ myo51::ura4$^+$ ade6-M216 leu1-32 ura4-D18*	Laboratory stock
2537	*h$^+$ myo51::ura4$^+$ leu1-32 ura4-D18*	This study
2538	*h$^-$ myo52::ura4$^+$ myo51::ura4$^+$ ade6$^-$ ura4-*	This study
2539	*h$^+$ myo52::ura4$^+$ myo51::ura4$^+$ leu1$^-$ ura4-*	This study
1024	*h$^-$ fus1::LEU2 ade6-*	Laboratory stock
1025	*h$^+$ fus1::LEU2 ade6-*	Laboratory stock
1273	*h$^-$ nmt41::GFP-CHD-leu$^+$ ade6-M216 leu1-32 ura4-D18*	Laboratory stock
663	*h$^+$ myo51::ura4$^+$ myo52::ura4$^+$ nmt41::GFP-CHD-leu$^+$ ade6-M216 leu1-32 ura4-D18*	Laboratory stock
2517	*h90 fus1-sfGFP-kanMX p^{map3}-tdTomato-ura4$^+$ ade6$^+$ leu1$^+$ ura4-D18*	This study
2541	*h90 myo52::ura4$^+$ fus1-sfGFP leu1$^-$ ura4-*	This study
2542	*h90 myo51::ura4$^+$ fus1-sfGFP leu1$^-$ ura4-*	This study
2543	*h90 myo52::ura4$^+$ myo51::ura4$^+$ fus1-sfGFP leu1$^-$ ura4-*	This study
2544	*h90 myo52::ura4$^+$ leu1$^-$ ura4-*	This study
2545	*h90 myo51::ura4$^+$ leu1$^-$ ura4-*	This study
1396	*h90 WT (968)*	Laboratory stock
2546	*h$^-$ myo52$^{\Delta tail}$-tdTomato-kanMX ade6-M210 leu1-32 ura4-D18*	Lo Presti et al., 2012

Table S1. **Strains used in this study** *(Continued)*

Strain number	Genotype	Source
2005	*h⁻ myo51$^{\Delta tail}$-3GFP-ura4⁺ ade6-M216 leu1⁻ ura4-*	Lo Presti et al., 2012
Fig. 5		
2547	*h⁻ agn1-GFP-kanMX myo52-tdTomato-natMX ade6-M216 leu1-32 ura4-D18*	This study
2548	*h⁺ agn1-GFP-kanMX myo52-tdTomato-natMX ade6-M216 leu1-32 ura4-D18*	This study
2549	*h⁻ agn2-GFP-kanMX myo52-tdTomato-natMX ade6-M216 leu1-32 ura4-D18*	This study
2550	*h⁺ agn2-GFP-kanMX myo52-tdTomato-natMX ade6-M216 leu1-32 ura4-D18*	This study
2551	*h⁻ eng1-GFP-kanMX myo52-tdTomato-natMX ade6-M216 leu1-32 ura4-D18*	This study
2552	*h⁺ eng1-GFP-kanMX myo52-tdTomato-natMX ade6-M216 leu1-32 ura4-D18*	This study
2553	*h⁻ eng2-GFP-kanMX myo52-tdTomato-natMX ade6-M216 leu1-32 ura4-D18*	This study
2554	*h⁺ eng2-GFP-kanMX myo52-tdTomato-natMX ade6-M216 leu1-32 ura4-D18*	This study
2555	*h⁻ exg1-GFP::kanMX myo52-tdTomato-natMX ade6-M216 leu1-32 ura4-D18*	This study
2556	*h⁺ exg1-GFP::kanMX myo52-tdTomato-natMX ade6-M216 leu1-32 ura4-D18*	This study
2557	*h⁻ exg2-GFP::kanMX myo52-tdTomato-natMX ade6-M216 leu1-32 ura4-D18*	This study
2558	*h⁺ exg2-GFP::kanMX myo52-tdTomato-natMX ade6-M216 leu1-32 ura4-D18*	This study
2559	*h⁻ exg3-GFP::kanMX myo52-tdTomato-natMX ade6-M216 leu1-32 ura4-D18*	This study
2560	*h⁺ exg3-GFP::kanMX myo52-tdTomato-natMX ade6-M216 leu1-32 ura4-D18*	This study
2561	*h⁻ agn1::ura4⁺ myo52-tdTomato-natMX ade6-M216 leu1-32 ura4-D18*	This study
2562	*h⁻ agn2::kanMX myo52-tdTomato-natMX ade6-M216 leu1-32 ura4-D18*	This study
2563	*h⁻ eng1::kanMX myo52-tdTomato-natMX ade6-M216 leu1-32 ura4-D18*	This study
2564	*h⁻ eng2::kanMX myo52-tdTomato-natMX ade6-M216 leu1-32 ura4-D18*	This study
2195	*h⁻ exg1::kanMX leu1-32*	Dueñas-Santero et al., 2010
2565	*h⁻ exg2::kanMX myo52-tdTomato-natMX ade6-M216 leu1-32 ura4-D18*	This study
2566	*h⁻ exg3::kanMX myo52-tdTomato-natMX ade6-M216 leu1-32 ura4-D18*	This study
2567	*h⁻ eng2::kanMX agn2::kanMX myo52-tdTomato-natMX ade6-M216 leu1-32 ura4-D18*	This study
2595	*h⁺ exg3::kanMX agn2::kanMX myo52-tdTomato-natMX ade6-M216 leu1-32 ura4-D18*	This study
2568	*h⁻ exg3::kanMX agn2::kanMX myo52-tdTomato-natMX ade6-M216 leu1-32 ura4-D18*	This study
2569	*h⁻ exg3::kanMX eng2::kanMX myo52-tdTomato-natMX ade6-M216 leu1-32 ura4-D18*	This study
2570	*h⁻ exg3::kanMX eng2::kanMX agn2::kanMX ade6-M216 leu1-32 ura4-D18*	This study
1088	*h⁻ bgs1::ura4⁺ P^{bgs1}:GFP-bgs1-leu1⁺ leu1-32 ura4-D18 his3-D1*	Cortés et al., 2002
806	*h⁻ bgs4::ura4⁺ P^{bgs4}:GFP-bgs4-leu1⁺ leu1⁻ ura4-D18*	Cortés et al., 2005
2571	*h90 agn2-sfGFP-kanMX myo52-tdTomato-natMX ade6-M216 leu1-32 ura4-D18*	This study
2572	*h90 eng2-sfGFP-kanMX myo52-tdTomato-natMX ade6-M216 leu1-32 ura4-D18*	This study
2573	*h90 exg3-sfGFP-kanMX myo52-tdTomato-natMX ade6-M216 leu1-32 ura4-D18*	This study
2574	*h90 agn2-sfGFP-kanMX myo52-tdTomato-natMX fus1Δ::LEU2 ade6⁺ leu1-32 ura4-294*	This study
2575	*h90 eng2-sfGFP-kanMX myo52-tdTomato-natMX fus1Δ::LEU2 ade6⁺ leu1-32 ura4-294*	This study
2576	*h90 exg3-sfGFP-kanMX myo52-tdTomato-natMX fus1Δ::LEU2 ade6⁺ leu1-32 ura4-294*	This study
2577	*h90 myo52::ura4⁺ myo51::ura4⁺ agn2-sfGFP-kanMX leu1⁻ ura4-*	This study
2578	*h90 myo52::ura4⁺ myo51::ura4⁺ eng2-sfGFP-kanMX leu1⁻ ura4-*	This study
2579	*h90 myo52::ura4⁺ myo51::ura4⁺ exg3-sfGFP-kanMX leu1⁻ ura4-*	This study
952	*h⁻ myo52-tdTomato-natMX ade6-M216 leu1-32 ura4-D18*	Laboratory stock
2580	*h⁺ myo51$^{\Delta tail}$-12myc-ura4⁺ agn2-sfGFP-kanMX ade6⁺ leu1-32 ura4-D18*	This study
2581	*h⁺ myo52$^{\Delta tail}$-tdTomato-kanMX agn2-sfGFP-kanMX ade6-M216 leu1-32 ura4-D18*	This study
2582	*h⁺ myo51$^{\Delta tail}$-12myc-ura4⁺ eng2-sfGFP-kanMX ade6⁺ leu1-32 ura4-D18*	This study
2583	*h⁺ myo52$^{\Delta tail}$-tdTomato-kanMX eng2-sfGFP-kanMX ade6-M216 leu1-32 ura4-D18*	This study
2584	*h⁺ myo51$^{\Delta tail}$-12myc-ura4⁺ exg3-sfGFP-kanMX ade6⁺ leu1-32 ura4-294*	This study
2585	*h⁺ myo52$^{\Delta tail}$-tdTomato-kanMX exg3-sfGFP-kanMX ade6-M216 leu1-32 ura4-D18*	This study
Fig. S1		
1396	*h90 WT (968)*	Laboratory stock
1442	*h90 fus1::LEU2 leu1⁻ ura4-D18*	Laboratory stock
2596	*h90 nmt41::lifeact-GFP-leu⁺ ade6⁻ leu1-32 ura4-D18*	This study
2586	*h90 fus1::LEU2 nmt41::lifeact-GFP ade6⁻ leu1-32 ura4-D18*	This study
Fig. S2		
2514	*h90 p^{map3}-tdTomato-ura4⁺ nmt41::GFP-CHD-leu⁺ ade6⁻ leu1-32 ura4-D18*	This study
2522	*h90 for3::kanMX nmt41::GFP-CHD-leu⁺ ade6⁻ leu1-32 ura4-D18*	This study
2587	*h90 for3::kanMX fus1::LEU2 nmt41::GFP-CHD-leu⁺ ade6⁻ leu1-32 ura4-D18*	This study
2597	*h90 dip1::natMX nmt41:GFP-CHD leu⁺ ade6⁻ leu1-32 ura4-D18*	This study
2598	*h90 vrp1::kanMX nmt41:GFP-CHD ade6-M216 leu1-32 ura4-D18 his3-D1*	This study
2599	*h⁻ vrp1::kanMX myo52-tdTomato-natMX ade6⁻ leu1-32 ura4-D18*	This study
1944	*h⁻ dip1::natMX ade6-M216 leu1-32 ura4-D18*	Basu and Chang, 2011

Table S1. **Strains used in this study** *(Continued)*

Strain number	Genotype	Source
1055	*h⁻ for3::kanMX ade6⁻ leu1-32 ura4-D18*	Laboratory stock
2588	*h90 cdc12-112 nmt41::GFP-CHD-leu⁺ ade6⁻ leu1-32 ura4-D18*	This study
2589	*h90 for3::kanMX cdc12-112 nmt41::GFP-CHD-leu⁺ ade6⁻ leu1⁻ ura4-D18*	This study
2590	*h90 for3::kanMX cdc12-112 fus1::LEU2 nmt41::GFP-CHD-leu⁺ ade6⁻ leu1-32 ura4-D18*	This study
2173	*h⁻ leu1::nmt41-GFP-cdc8-ura4⁺ ura4-D18*	Skau et al., 2011
2591	*h⁻ rlc1-GFP-kanMX leu1⁻ ura4-*	This study
2163	*h⁻ arc5-mGFP-kanMX ade6-M216 leu1-32 ura4-D18 his3-D1*	Arasada and Pollard, 2011
2194	*h90 cam2::ura4⁺ ade6<<cam2-GFP leu1-32 ura4-D18*	Itadani et al., 2006
2161	*h⁻ kanMX-P^{wsp1}-mGFP-wsp1 ade6-M216 leu1-32 ura4-D18 his3-D1*	Arasada and Pollard, 2011
2592	*h90 crn1-tdTomato-natMX nmt41::GFP-CHD-leu⁺ ade6⁻ leu1-32 ura4-D18*	This study
740	*h⁺ myo52-tdTomato-natMX ade6-M216 leu1-32 ura4-D18*	Laboratory stock
Fig. S3		
2520	*h90 myo52-GFP-kanMX leu1-32*	This study
2521	*h90 fus1::LEU2 myo52-GFP-kanMX leu1-32*	This study
2529	*h90 myo52-tdTomato-natMX myo51-3YFP-kanMX leu1-32 ura4-D18*	This study
2593	*h90 myo51-3YFP-kanMX fus1::LEU1 ade6-M216 leu1-32 ura4-D18*	This study

All tagging constructs are in frame after the last codon of the gene or before the first one and integrated at the endogenous genomic locus. All deletions are replacements of the complete gene ORF with the selectable marker. The *p^{map3}*-driven transgenes are integrated in the *map3* promoter locus. WT, wild type.

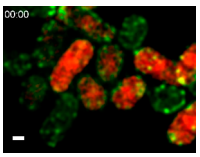

Video 1. **An actin fusion focus forms before cell fusion.** (Related to Fig. 1.) Time lapse of homothallic *h90 p^{map3}:tdTomato GFP-CHD* strain obtained by wide field microscopy and deconvolved using the DeltaVision platform (Olympus IX-71; Applied Precision). CHD-GFP is shown in green; tdTomato in red. Time interval is 2 min. The video is sped up sevenfold. Three distinct mating pairs can be seen fusing during the course of the video. Note formation of the fusion focus before fusion, entry of the red signal in the *h⁺* cell at fusion time and focus disassembly after fusion. Bar, 1 µm.

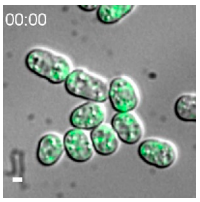

Video 2. **Absence of actin fusion focus in *fus1Δ*.** (Related to Fig. 1.) Time-lapse of homothallic *h90 fus1Δ GFP-CHD* strain obtained by wide field microscopy and deconvolved using the DeltaVision platform (Olympus IX-71; Applied Precision). CHD-GFP is shown in green; differential interference contrast image in gray. Time interval is 2 min. The video is sped up sevenfold. Four distinct mating pairs can be seen, all of which fail to fuse. Instead, mating partners keep growing in a polarized fashion toward each other. Actin structures, likely actin patches can be seen dynamically localizing at the shmoo tip, but no long-lasting actin focus is observed. Note the GFP-CHD channel has been contrasted to allow visibility on the differential interference contrast image. Bar, 1 µm.

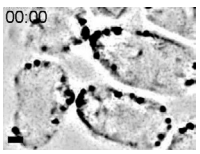

Video 3. **The actin fusion focus visualized by 3D SIM.** (Related to Fig. 2.) Time-lapse of GFP-CHD in homothallic *h90 WT GFP-CHD myo52-tdTomato* cells. Only the GFP-CHD channel is shown. Inverted images are shown obtained using the SIM setup (Eclipse T1; Nikon). Time interval is 6 s. The video is sped up sevenfold. Long linear dynamic actin cables are observed originating from the zone of cell–cell contact. Contrast was adjusted to optimize cable visualization. Bar, 1 µm.

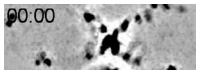

Video 4. **The actin fusion focus visualized by 3D SIM in *for3Δ*.** (Related to Fig. 2.) Time-lapse of homothallic *h90 for3Δ* GFP-CHD cells. Inverted images are shown obtained using the SIM setup (Eclipse T1; Nikon). Time interval is 3 s. The video is sped up sevenfold. Short linear dynamic actin cables are observed originating from the zone of cell–cell contact. Contrast was adjusted to optimize cable visualization. Bar, 1 µm.

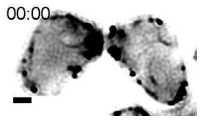

Video 5. **Actin at the zone of cell–cell contact visualized by 3D SIM in *fus1Δ*.** (Related to Fig. 2.) Time-lapse of homothallic *h90 fus1Δ* GFP-CHD cells. Inverted images are shown obtained using the SIM setup (Eclipse T1; Nikon). Time interval is 3 s. The video is sped up sevenfold. Long dynamic actin cables are observed emanating from a broad region at the cell–cell contact site. Contrast was adjusted to optimize cable visualization. Bar, 1 µm.

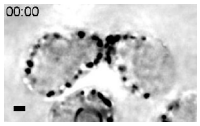

Video 6. **Actin at the zone of cell–cell contact visualized by 3D SIM in *fus1Δ for3Δ*.** (Related to Fig. 2.) Time-lapse of homothallic *h90 fus1Δ for3Δ* GFP-CHD cells obtained using the SIM setup (Eclipse T1; Nikon). Inverted images are shown. Time interval is 3 s. The video is sped up sevenfold. No actin cables were observed; however, a perinuclear actin ring is seen. Note that only part of this ring is visible because only a single focal plane is shown. Bar, 1 µm.

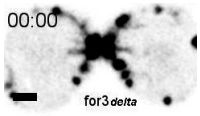

Video 7. **The actin fusion focus visualized by scanning confocal microscopy in WT and *for3Δ*.** (Related to Fig. 2.) Images of homothallic *h90 WT GFP-CHD myo52-tdTomato* (left) and *h90 for3Δ GFP-CHD* (right) cells obtained by laser-scanning confocal microscopy (LSM 710; Carl Zeiss). Only the GFP-CHD signal was imaged to minimize the time interval (2 s). The video is sped up sevenfold. Long and short actin cables are observed originating from the zone of cell–cell contact in WT cells, and short linear actin cables are observed in *for3Δ* cells. Contrast was adjusted to optimize cable visualization. Bar, 1 µm.

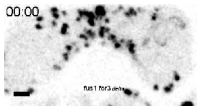

Video 8. **Actin at the zone of cell–cell contact visualized by scanning confocal microscopy in *fus1Δ* and *fus1Δ for3Δ*.** (Related to Fig. 2.) Images of homothallic *h90 fus1Δ GFP-CHD* (left) and *h90 fus1Δfor3Δ GFP-CHD* (right) cells obtained by laser-scanning confocal microscopy (LSM 710; Carl Zeiss). Time interval is 2 s. The video is sped up sevenfold. Long dynamic, unfocalized actin cables are observed in *fus1Δ*. No actin cables were observed in *fus1Δ for3Δ*. Contrast was adjusted to optimize cable visualization. Bar, 1 µm.

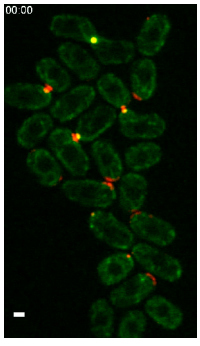

Video 9. **Asymmetric maturation of the fusion focus.** (Related to Fig. 3.) Time-lapse of homothallic *h90 WT myo52-tdTomato myo51-3YFP* obtained by spinning disk microscopy (UltraVIEW system [PerkinElmer] on DMI4000B [Leica]). Myo52-tdTomato is shown in red; Myo51-3YFP is shown in green. Time interval is 1.3 s. The video is sped up sevenfold. The video shows five mating pairs at distinct stages of the fusion process. Pair 1 shows Myo52-tdTomato crescent in both partner cells, with the bottom cell structure focalizing in the course of the video. Pairs 2, 3, and 4 show asymmetric structures, with Myo51-3YFP strongly focalized with Myo52-tdTomato in only one of the two mating partners. Note how the Myo52-tdTomato structure in the other cell moves at the contact zone relative to that stable focus. In the course of the video, Myo51-3YFP accumulates in the focus of the bottom cell of pair 4. Finally, pair 5 shows a single Myo51-Myo52 focus at the fusion site, which disassembles in the course of the video. Bar, 1 µm.

References

Arasada, R., and T.D. Pollard. 2011. Distinct roles for F-BAR proteins Cdc15p and Bzz1p in actin polymerization at sites of endocytosis in fission yeast. *Curr. Biol.* 21:1450–1459. http://dx.doi.org/10.1016/j.cub.2011.07.046

Basu, R., and F. Chang. 2011. Characterization of dip1p reveals a switch in Arp2/3-dependent actin assembly for fission yeast endocytosis. *Curr. Biol.* 21:905–916. http://dx.doi.org/10.1016/j.cub.2011.04.047

Cortés, J.C., J. Ishiguro, A. Durán, and J.C. Ribas. 2002. Localization of the (1,3)beta-D-glucan synthase catalytic subunit homologue Bgs1p/Cps1p from fission yeast suggests that it is involved in septation, polarized growth, mating, spore wall formation and spore germination. *J. Cell Sci.* 115:4081–4096. http://dx.doi.org/10.1242/jcs.00085

Cortés, J.C., E. Carnero, J. Ishiguro, Y. Sánchez, A. Durán, and J.C. Ribas. 2005. The novel fission yeast (1,3)beta-D-glucan synthase catalytic subunit Bgs4p is essential during both cytokinesis and polarized growth. *J. Cell Sci.* 118:157–174. http://dx.doi.org/10.1242/jcs.01585

Dueñas-Santero, E., A.B. Martín-Cuadrado, T. Fontaine, J.P. Latgé, F. del Rey, and C. Vázquez de Aldana. 2010. Characterization of glycoside hydrolase family 5 proteins in *Schizosaccharomyces pombe*. *Eukaryot. Cell*. 9:1650–1660. http://dx.doi.org/10.1128/EC.00187-10

Itadani, A., T. Nakamura, and C. Shimoda. 2006. Localization of type I myosin and F-actin to the leading edge region of the forespore membrane in *Schizosaccharomyces pombe*. *Cell Struct. Funct.* 31:181–195. http://dx.doi.org/10.1247/csf.06027

Lo Presti, L., F. Chang, and S.G. Martin. 2012. Myosin Vs organize actin cables in fission yeast. *Mol. Biol. Cell*. 23:4579–4591. http://dx.doi.org/10.1091/mbc.E12-07-0499

Skau, C.T., D.S. Courson, A.J. Bestul, J.D. Winkelman, R.S. Rock, V. Sirotkin, and D.R. Kovar. 2011. Actin filament bundling by fimbrin is important for endocytosis, cytokinesis, and polarization in fission yeast. *J. Biol. Chem.* 286:26964–26977. http://dx.doi.org/10.1074/jbc.M111.239004